Discovering a Novel AAV2-Based Capsid for RPE Transduction via Intravitreal Injection in *rd12* Mice for Leber Congenital Amaurosis Type 2 Gene Therapy

By

Sonali Singh

A dissertation submitted in partial satisfaction of the

requirements for the degree of

Doctor of Philosophy

in

Vision Science

in the

Graduate Division

of the

University of California, Berkeley

Committee in charge:

Professor John G. Flannery, Chair

Professor Teresa Puthussery

Professor Aparna Lakkaraju

Spring 2026

Discovering a Novel AAV2-Based Capsid for RPE Transduction via Intravitreal Injection in *rd12* Mice for Leber Congenital Amaurosis Type 2 Gene Therapy

By

Sonali Singh

Abstract

Discovering a Novel AAV2-Based Capsid for RPE Transduction via Intravitreal Injection in *rd12* Mice for Leber Congenital Amaurosis Type 2 Gene Therapy

by

Sonali Singh

Doctor of Philosophy in Vision Science

University of California, Berkeley

Professor John G. Flannery, Chair

Adeno-associated virus (AAV) mediated gene therapies for inherited retinal degenerations require precise targeting of the outer retina, particularly in the retinal pigment epithelium (RPE), which plays an essential role in maintenance of the light-sensitive neuron, photoreceptors. Mutations in RPE-expressed genes, including *RPE65*, lead to blinding diseases such as Leber congenital amaurosis type 2 (LCA2). While subretinal injection achieves optimal RPE transduction, it is an invasive, inpatient surgical procedure associated with iatrogenic damage, including retinal detachment. Intravitreal (IVT) surgery is a far less invasive, outpatient procedure but has previously been shown to have limited penetration of the inner limiting membrane (ILM) of the retina and thus poor outer retina transduction. The goal of this study is to identify capsid variants capable of overcoming this barrier. Here, high-throughput screenings of libraries of over 1.28×10^9 capsids from different AAV serotypes were conducted, each with different outer surface structures to alter their binding properties, to be delivered with IVT injection in mice. Parallel screens were conducted in non-human primate (NHP) macaque and canine models for cross-species validation and better clinical translatability. A novel AAV serotype 2 based capsid, "Variant 3" (AAV2.Var3) was found to transduce approximately 10% of RPE cells in mouse and NHP eyes. For comparison, a leading, clinical-stage vector that is also AAV2-based, 7m8, effectively transduces the outer retina but has limited success targeting RPE through IVT delivery, where only 0-1% transduction was seen in this study. Previous studies have also determined a lack of RPE transduction with AAV2.7m8 IVT delivery in primates.

To test the therapeutic efficacy of Variant 3, a therapeutic gene, human *RPE65* (h*RPE65*), was packaged in AAV2.Var3, driven in expression by ubiquitous (*CAG*) and RPE-specific (*BEST1*)

promoters. These constructs were injected intravitreally at postnatal day 14 (P14) in *rd12* mice, a disease model for Leber congenital amaurosis type 2 (LCA2). AAV2.Var3-h*RPE65* treated cohorts showed an increase in RPE65 protein expression confirmed by immunohistochemistry and Western blot. There was also a recovery of retinoid production evidenced by high-performance liquid chromatography (HPLC) assays to quantify 11-*cis*-retinal and all-*trans*-retinyl ester. Visual function assessed by both scotopic and photopic electroretinography (ERG) in response to light flashes demonstrated a slight improvement in rod-mediated visual function. With the translational feasibility of the AAV2.Var3 capsid, supported by demonstrated RPE transduction in the primate model following IVT delivery, these findings establish AAV2.Var3 as a promising vector for minimally invasive IVT gene delivery to the RPE, with potential clinical application in LCA2 and other RPE-associated inherited retinal diseases.

Table of Contents

List of Figures

Chapter 1

Chapter 2

Acknowledgments

If John Flannery had not taken a chance on a twenty-three-year-old with more enthusiasm than experience, I would not be where I am today. I attribute the entirety of my enjoyment of the Ph.D. experience in the Vision Science program at UC Berkeley to his mentorship and leadership. There was never a moment in this lab where I did not feel fully encouraged, supported, and valued. John's mentorship extends well beyond scientific training and research direction. It encompasses wisdom that is delivered through fun anecdotes that somehow manage to address every obstacle, large or small, while keeping the student's wellbeing and confidence at the center. He graciously supported my travel to conferences in Spain and the Czech Republic, where some of my proudest moments as a scientist took place. Above all, John has consistently ensured that the mental health and happiness of his students came first, and it is this quality, more than any other, that made my time in his lab so meaningful, successful, and deeply fulfilling. I feel confident about my future as a scientist because of him and will always be so thankful.

The hardest part of completing this chapter of my life is no longer having my desk beside Meike Visel. Having her as my lab manager for the past five years was nothing short of extraordinary. She ensured that my experiments were always well-supplied and progressing, that my spirits were kept high during the difficult stretches, and that I always had someone to turn to. Beyond her exceptional professional role, I have gained in Meike a friend for life. She is, in every sense of the phrase, the heart and the "mom" of the Flannery lab. I am grateful for the memories, the laughter, and the guidance she has given me over the years.

To my lab mates, Beatrice Le, Lobna Hamed, and Poorna Sharma, thank you for the immeasurable ways you supported me, often without realizing the depth of your impact. Sharing the struggles, the breakthroughs, and the full emotional range of this journey with you has made my experience truly special. You have also all inspired me to be a better scientist in many ways. You each have so much light radiating within you that I am lucky to be taking a part of that with me to wherever I go next. I have found in each of you a lifelong friend as well, and I will cherish that deeply. I wish you every success in the chapters of your Ph.D. that remain, and I hope you know that my support and assistance are always available in whatever lies ahead.

Thank you to our honorary lab member, Scott Geller, who taught me such an invaluable range of technical skills that I will carry with me to every lab I work in going forward. His thoroughness, precision, and breadth of expertise are admirable, and I feel fortunate to have learned so much under his guidance. The lab is deeply grateful for his willingness to lend his expertise despite simultaneously pursuing many other impactful endeavors.

Thank you to the undergraduate and high school students I had the privilege of mentoring over the years: Monica Stapor, Cecilia Hu, Aneal Singh, Sabrina Spatny, Naomi Leader, Penny Reynolds, Beth Wade, Vivian Tran, and Tyler Houston. Every hour spent working alongside you taught me as much about science and about myself as it did about mentorship. You have each left a meaningful mark on my scientific career and reminded me, time and again, why this work matters. I hope you pursue your goals with the same dedication and warmth you brought to the lab; you are all exceptionally deserving. Thank you for making lab so much fun!

I would also like to extend my sincere gratitude to our collaborators on this project. Thank you to Krzysztof Palczewski and Zachary Engfer at UC Irvine for generously collecting HPLC data on our behalf. Thank you to Leah Byrne, lab alumna and a constant source of guidance, for allowing me to utilize the canine and NHP DNA samples that became such valuable components of my library screening results, and for her patience in answering my many questions throughout the years. Thank you to lab alumni, Bilge Esin Ozturk and Timothy Day, for the immense protocol design assistance they provided during my first year. Lastly, thank you to Ala Moshiri and Guillaume Luxardi at UC Davis for so generously testing our AAV vector in a non-human primate model, a contribution that substantially strengthened and validated the findings of this dissertation.

Finally, I would like to acknowledge the wonderful community of mentors who have inspired and guided me throughout this journey. Thank you to Teresa Puthussery for being a model of excellence and integrity. Thank you to Aparna Lakkaraju for holding me to a high standard and believing in my abilities. All your confidence in me has shaped me into a more rigorous and capable researcher than I would otherwise have become. Lastly, thank you to Cathy Bowes Rickman for your thoughtful guidance and scientific direction throughout the inception of this project. You have dedicated immense time to ensuring my success in this project. I appreciate all your mentorship during your time as my honorary 4th thesis committee member.

Dedication

To Akhil, my soon-to-be husband, for being my foundation whenever the ground felt unsteady, my most trusted confidant through every difficulty, and my best friend.

To Aruna, my mother, who recognized something in me long before I recognized it in myself, and whose encouragement throughout every academic and creative endeavor of my life made this one possible.

To Alok, my father, for always making me feel more capable and more brilliant than I ever did on my own. Your faith in me to achieve great things is why I have never been afraid to try.

Chapter 1 Introduction

1.1 AAV-Mediated Gene Therapy

Gene therapy is a rapidly advancing therapeutic technique that has proven to be effective in clinical trials for several diseases, such as leukemia, hemophilia, and severe combined immune deficiency.[1,2] This therapeutic strategy can be used to treat patients with inherited diseases with genetic mutations that lead to severe health disparities. While gene therapy comes in many forms, the gene therapy modality addressed in this dissertation is a subclass pertaining to gene augmentation, where a new, functional copy of a gene is added to a cell for transcription and translation. In the case of a patient where a gene is miscoded, thus leading to a dysfunctional protein and disease pathogenesis, gene augmentation allows for restoration of proper gene and functional protein expression.

Gene augmentation can be performed using an adeno-associated viral capsid as a vehicle to deliver up to 4.7 kilobases of genetic material to a cell. In 1965, the first wildtype adeno-associated virus (AAV) was discovered and characterized as a non-pathogenic parvovirus that is highly present in our natural environment.[3] Coupled with a helper virus, from the adenovirus family, an AAV can replicate. Humans develop neutralizing antibodies against this virus at an early age, making AAV infections relatively harmless. Packaged inside the icosahedral AAV capsid is single-stranded DNA encoding genes for replication (Rep) and capsid structure (Cap). Both the Rep and Cap sequences are flanked by inverted terminal repeat sequences (ITRs), approximately 130-150 base pairs (bp) in length. The Cap sequence is divided into three sections, VP1, VP2, and VP3, each encoding for a protein that makes up part of the whole capsid. The capsid sequence is what determines the binding and transduction properties of the capsid. To date, 13 serotypes have been thoroughly characterized and found to all differ slightly in the outer surface structure.[2,4-6] Importantly, capsid binding affinity to cell surface receptors like heparan sulfate proteoglycan (HSPG) and fibroblast growth factor receptor (FGFR) can be modified.[7-9] Once assembled, a singular AAV capsid has a diameter of just 25 nm.[10]

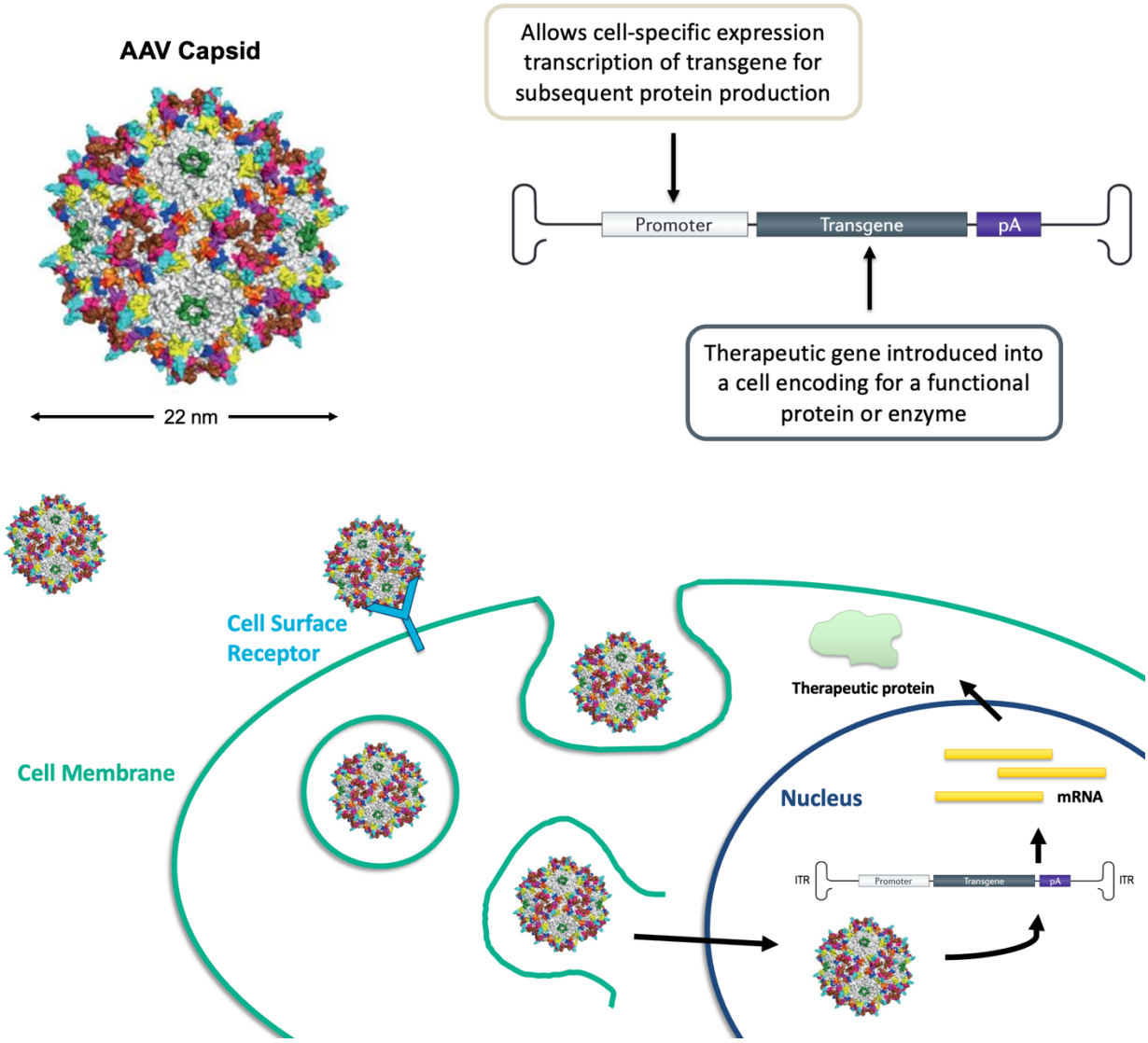

Figure 1.1.1 *Adeno-associated viral capsid and the process of cellular transduction.* (Top left) Pictured is an adeno-associated viral capsid. Hypervariable regions of the VP3 sequence that encode the capsid structure are represented as colored regions of the capsid. Different serotypes of AAVs present different structures at these colored regions. (Top right) Within two ITRs is this single-stranded DNA that is packaged inside the capsid. (Bottom) A simplified representation of the process of cellular transduction of an AAV for therapeutic protein expression. Figure adapted from Kotterman (2014).

Scientists today are able to change the outer capsid conformation and replace the single-stranded DNA inside the capsid with a transgene that they wish to induce the expression of in a

targeted cell type.[11] These capsids bind to specific cell surface receptors and become endocytosed by the host cell. Upon migration into the cell nucleus, the virus sheds and degrades its capsid shell to release its single-stranded DNA.[12,13] This DNA is transcribed into a double stranded episome of DNA that stays resident to the cell nucleus with stability, due to the presence of ITRs. With this, mRNA can be transcribed and functional protein can be translated continuously.[2] Cell-specific gene expression can be controlled with the addition of a cell-specific promoter sequence preceding the transgene.

For a disease application in tissue where cell turnover is high and cells are actively undergoing their mitotic cycle, AAV-mediated gene augmentation is not effective.[14] So, other forms of gene therapy can be utilized including gene silencing by RNA interference and gene editing most performed by a CRISPR-Cas9 system. The inability to perform gene augmentation on dividing cells is because the episomal DNA from the AAV does not carry over to daughter cells of the primary host. Due to this phenomena, AAV-mediated gene therapy is best conducted in tissue where cells are post-mitotic or no longer undergoing cell death, like in the central nervous, cardiovascular, and musculoskeletal systems. Retinal tissue at the back of the mammalian eye is part of this subgroup of non-dividing cells. On the one hand, the post-mitotic nature of retinal neurons precludes regeneration and repair in the context of retinal degeneration. On the other hand, this property is beneficial because inducing the expression of a therapeutic gene in a subset of retinal cells will provide long lasting gene expression. Clinically, longevity of gene expression means a reduced number of visits to the surgery room for injection, which is desirable for patients and reduces the risk of injection-associated complications. In this way, AAV-mediated gene therapy for retinal degenerative diseases is an attractive avenue for therapeutic development.

1.2 The Retina

Vision is one of the most essential senses involving complex neuronal signaling along the back of the eye before visual information is sent to the brain for further processing. Light from our natural environment enters the eyeball through the cornea, which is the first transparent, multi-layered tissue at the forefront of the eye (Figure 1.2.1). The light is then narrowed through the pupil, a small opening at the center of the iris, and passes through the vitreous, a viscous fluid filling the center of the eyeball, before it reaches the retina. Most of the light that reaches the retina is focused on the central region called the macula.

The retina is a thin layer of neurons, supportive glial cells, and an epithelium, that coats the back wall of the eye, averaging around 250-300 μm thick. Within the retina specifically, light first passes through the inner limiting membrane, which acts as a barrier between the vitreous and the retina. The retina is organized into alternating layers of neuronal cell bodies, or nuclear layers, and synaptic connections between them, or plexiform layers. Traveling from the inner retina to the outer retina, the retinal ganglion cells occupy the ganglion cell layer (GCL), and their axons form the nerve

fiber layer that exits the eye at the optic disc, extending to the brain. The inner plexiform layer (IPL) then separates the GCL from the inner nuclear layer (INL), which houses the interneurons of the retina: amacrine cells, bipolar cells, and horizontal cells, as well as the cell bodies of Müller glia. The outer plexiform layer (OPL) forms the next synaptic zone, where photoreceptor terminals contact bipolar and horizontal cell dendrites. The outer nuclear layer (ONL) contains the photoreceptor cells, rods and cones, whose outer segments extend toward the retinal pigment epithelium (RPE). This epithelial layer sits at the outermost boundary of the retina and provides essential metabolic support to the photoreceptors.[15]

Visual transduction begins when photons of light are captured by opsins containing a molecule called a chromophore which changes its conformation upon photon collection. There are around 150 million opsins sitting within the outer segment discs of rod and cone photoreceptors, waiting to be activated by a photon. Chromophore activation triggers the initiation of the phototransduction cascade which ultimately leads to the closure of cyclic-nucleotide gated cation channels at the membrane of the photoreceptor. The resulting reduction of sodium and calcium entry into the neuron leads to the internal charge becoming more negative, thus leading to hyperpolarization. Hyperpolarization causes a reduced amount of glutamate signaling to the downstream neurons, the bipolar cells. Otherwise, glutamate is constantly being sent from the photoreceptors to the bipolar cells while in a depolarized state. The reduced glutamate signaling to the bipolar cell is an indication that light has been detected and the signaling cascade continues to retinal ganglion cells and then eventually to the lateral geniculate nucleus (LGN) within the thalamus of the brain. Visual information is then relayed to the visual cortex of the brain for processing.[16]

The centermost, 300 μm region of the macula, called the foveola, has roughly 100,000-324,000 cone photoreceptors/mm^2, allowing for high acuity, trichromatic color vision.[17,18] Additionally, cones are the primary players in bright light conditions. Rod photoreceptors are not present in the foveola but are at a peak concentration at around 20 degrees of eccentricity outside the foveola, called the perifovea.[19] Rod numbers slowly decline as eccentricity increases, yet still make up 95% of the total photoreceptor population. Rods mediate vision in dim light conditions due to their increased sensitivity to photons and provide monochromatic visual information.

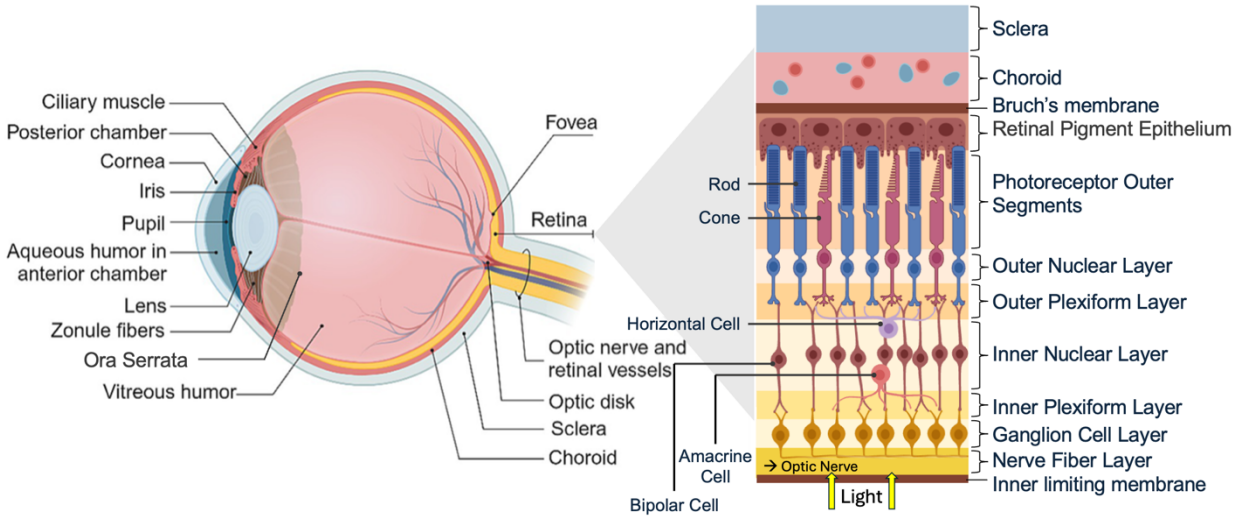

Figure 1.2.1 *Structure of the eye and the retina.* (Left) Sagittal cross section of a human eye, where light would first pass the cornea and aqueous humor before narrowing through the pupil opening. Lining the back of the eye is the retina (yellow), starting from a transition point after the ciliary region, called the ora serrata. The retina continues within the optic nerve where ganglion cell axons extend to the brain. (Right) Sagittal cross section of the human retina. Light enters the eye and traverses the retina starting from the inner limiting membrane (bottom) to the retinal pigment epithelium (top). Not pictured are Müller glia cells which span from the ganglion cell layer to the inner nuclear layer. Figure adapted from Stoddart (2024)[20], created in Biorender.com (2026).

Photoreceptors are constantly absorbing photons leading to high energy expenditure and need to be well supported for survival and maintenance. The retinal pigment epithelium (RPE) is what supports photoreceptors by transferring nutrients, oxygen, and ions.[21] Anatomically, photoreceptor outer segments intercalate with the long apical processes of the RPE to provide more surface area for transfer of growth factors. An essential supporting role of the RPE for photoreceptors during light detection is the replenishing of the light-sensitive chromophore, 11-*cis*-retinal. During photon absorption in the outer segment, the chromophore changes conformation from 11-*cis*-retinal to all-*trans*-retinal. Enzymes within the RPE, primarily LRAT and RPE65, are responsible for converting all-*trans*-retinyl ester, the chromophore in its storage form, into 11-*cis*-retinol, which is eventually oxidized by 11-*cis*-retinol dehydrogenases back to 11-*cis*-retinal for more photon absorption in the photoreceptors.[22-24]

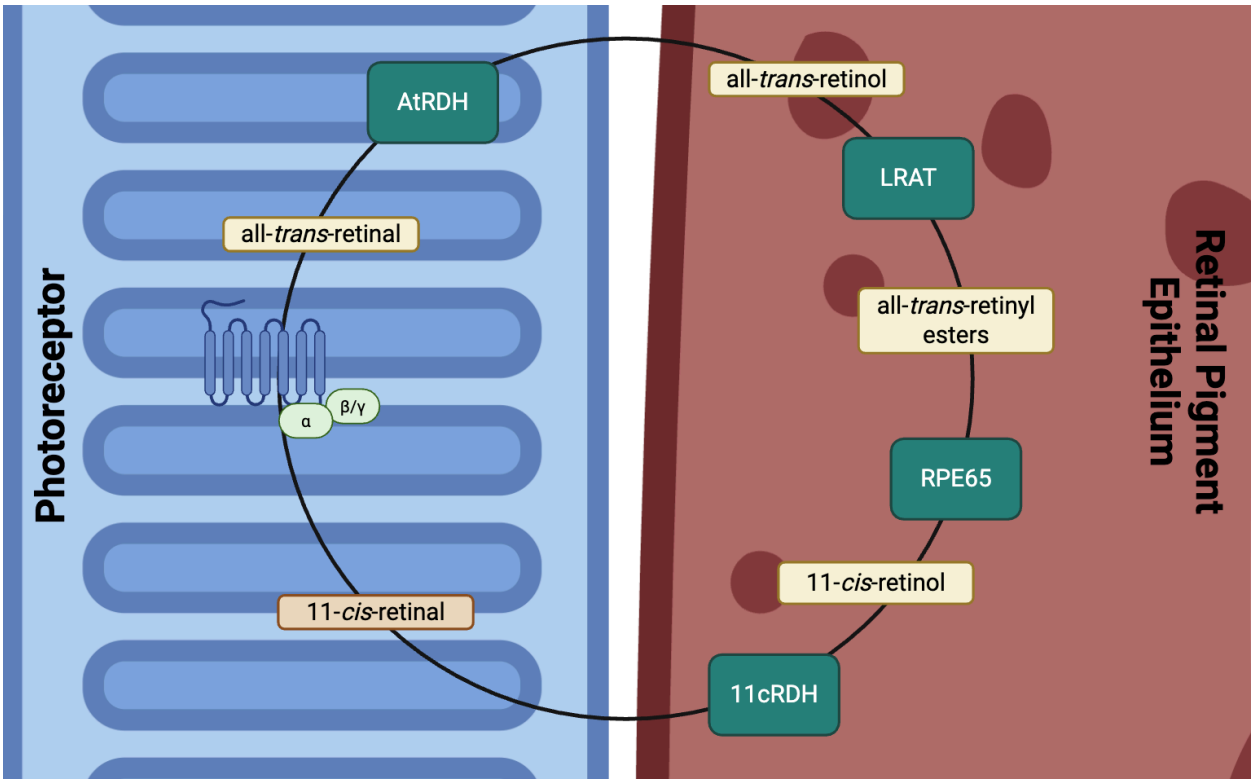

Figure 1.2.2 *The visual cycle.* The conversion of photoisomerized all-*trans*-retinal with the help of enzymes all-trans retinal dehydrogenase (AtRDH), lecithin retinol acyl transferase (LRAT), retinal pigment epithelium specific 65 kDa protein (RPE65), and 11-cis specific retinol dehydrogenase (11cRDH) back into 11-*cis*-retinal for light sensitivity and photon absorption. The transmembrane protein spanning the photoreceptor outer segment disc is rhodopsin, a G-protein coupled receptor where 11-*cis*-retinal sits before light activation. Not pictured here is how the conversion process in the RPE occurs primarily within the endoplasmic reticulum of the cell. Figure created with Biorender.com (2026).

Posterior to the RPE is the choroid where the innermost layer called the choriocapillaris, a dense single layered network of highly permeable fenestrated capillaries, located directly beneath Bruch's membrane, serving as the main outer retinal blood supply. This is the source of oxygen and nutrients for RPE and photoreceptors. The fenestrated endothelial cells lining the inner side of the choriocapillaris allow for ease of transfer of these elements. Between the RPE and choriocapillaris is the Bruch's membrane, a pentalaminar extracellular matrix, which acts as a molecular sieve, facilitating the exchange of nutrients and waste as well as providing structural support for the retina.

1.3 Retinal Degenerative Diseases

The overwhelming majority of inherited retinal diseases affect outer retinal cells, specifically photoreceptors and the RPE.[25,26] Mutations in these cell types lead to retinal dysfunction, rapid photoreceptor degeneration, and eventual loss of visual function.[16] One prominent example of outer retinal dysfunction is Leber Congenital Amaurosis (LCA), a group of severe dystrophies characterized by genetic mutations in genes essential to retinal development and function.[27] LCA type 2 (LCA2) results from biallelic loss-of-function mutations in the *RPE65* gene. Based on assays done in RPE65-deficient mice, patients with LCA2 are thought to accumulate all-*trans*-retinyl ester while their 11-*cis*-retinal levels are depleted.[28] Loss of RPE65 protein also leads to early-onset photoreceptor degeneration where surviving photoreceptors, primarily cones, lack light sensitivity.[29,30] Clinically, patients present with reduced vision, severe night blindness, nystagmus, and sluggish pupillary responses.[31]

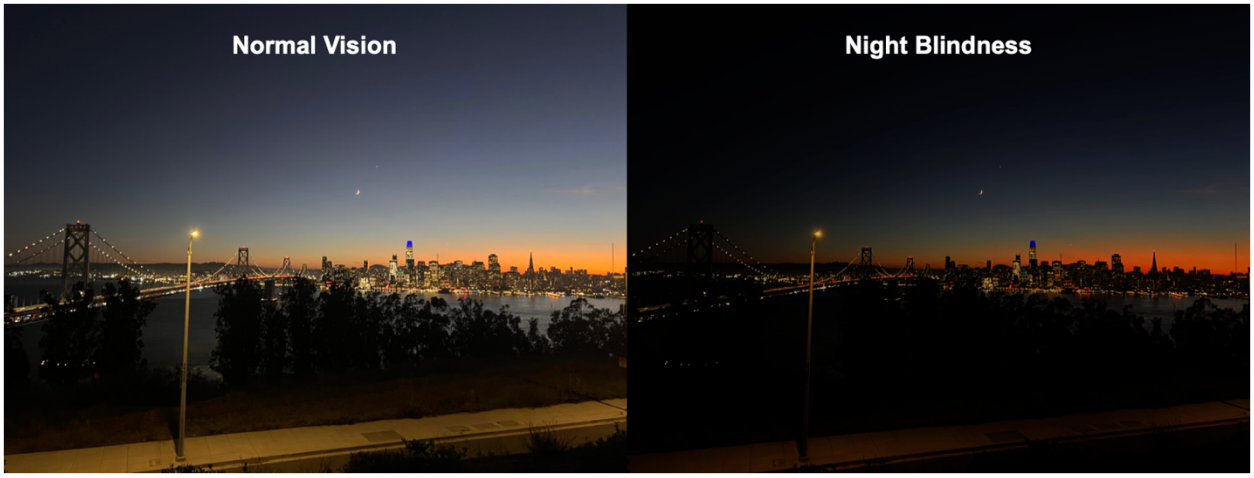

Figure 1.3.1 *Vision with night blindness.* This is a simulation of what a patient with LCA2 might see during dusk. In low light conditions, the patient's sensitivity to contrast in their visual environment is reduced.

The most prevalent retinal degenerative disease in the Western world is non-neovascular or dry age-related macular degeneration (AMD). Dry AMD is characterized by drusen deposit formation in the outermost layers of the retina, where pockets of lipoproteins and debris develop between the RPE and choroid within the inner collagenous layer of the Bruch's membrane, leading

to impermeable mounds. With this, essential nutrients and oxygen from the choroid cannot as readily reach the RPE causing RPE cell death and subsequent photoreceptor cell death, leading to geographic atrophy and eventual central vision loss. The exact cause of drusen formation and the RPE loss is unknown, but several genome-wide associated studies (GWAS) have been conducted, particularly among European-American patients over 60 years old diagnosed with dry AMD, to find commonalities in their genetic patterns.[32] The most frequent genetic trend among these patients included a variant in *CFH* where a tyrosine is switched for a histidine at position 402 in the AA sequence (Y402H).[33] Complement factor H (CFH) protein, is locally secreted by the RPE, and acts as the soluble regulator in an important immune process called the complement system where the ultimate goal is to initiate cell death on invading pathogens.[34] CFH works to prevent accidental cell death initiation on host cells by stopping activation of the alternative pathway of complement on their surfaces. The Y402H mutation decreases CFH protein's ability to bind to glycosaminoglycans, which are concentrated in the Bruch's membrane.[35] The possession of this risk allele of *CFH* increases the likelihood of dry AMD pathogenesis by a factor of 4.6 and 7.4 for those heterozygous and homozygous for the allele, respectively.[36]

Both LCA2 and dry AMD are examples of retinal degenerative diseases that are associated with genetic mutations or risk variants, respectively, which affect outer retinal cells like the RPE and photoreceptors. Diseases like these can benefit greatly from gene therapy strategies, where viral capsids can deliver the correct form of the affected gene to a target cell for functional restoration and/or gene augmentation.

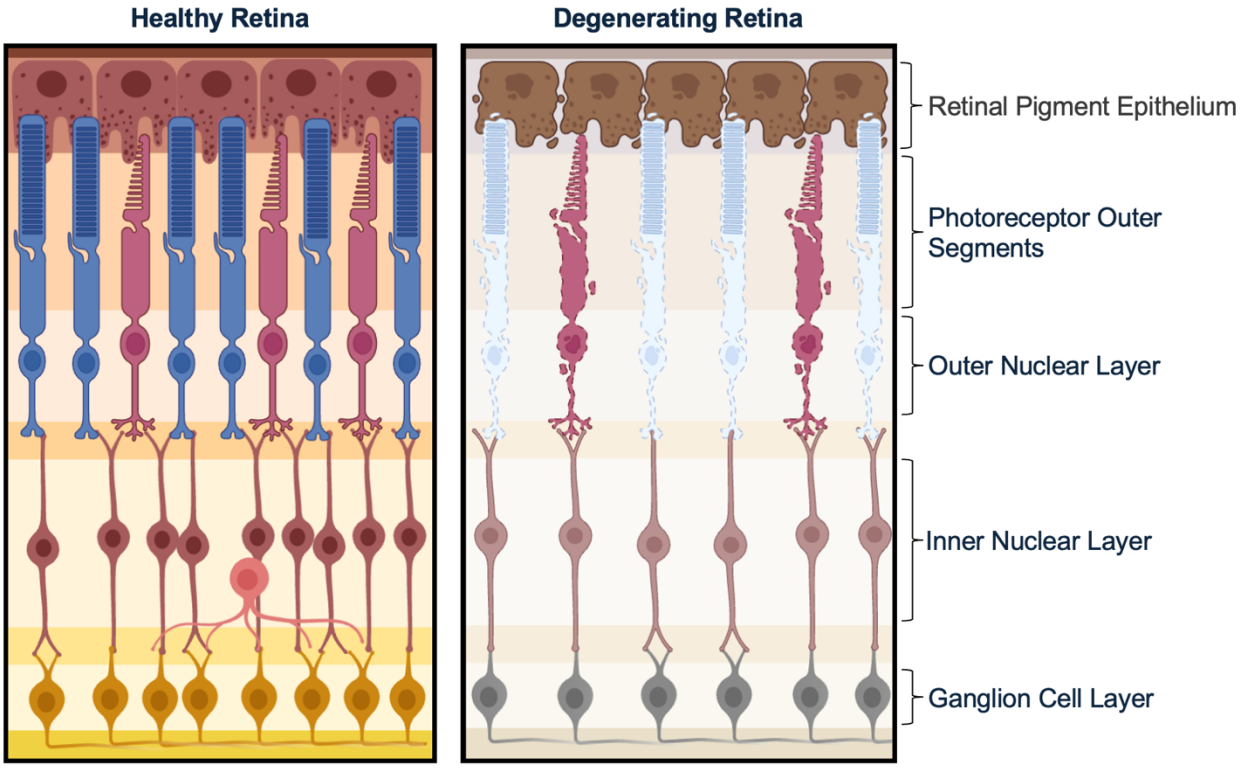

Figure 1.3.2 *Cell death during retinal degeneration.* Presented here is an example of what retinal degeneration can look like between the neuronal layers. Here we see reduced numbers of neurons creating gaps in the visual field where photons are no longer being captured. Often, remaining neurons and RPE are dysfunctional. Retinal degenerative diseases can also see a reduced number of RPE cells, breaking the blood retinal barrier and leading to neovascularization between the retinal neurons. Some of these blood vessels are known to advance cell death or even leak fluids. Figure created with Biorender.com (2026)

1.4 Limitations of AAV2 Delivery in the Retina

1.4.1 Heparan Sulfate Binding Motif on AAV Serotype 2

Currently, subretinal injection is the most utilized surgical procedure for delivery of AAV capsids to the outer retina for in vivo studies in the context of retinal diseases.[37,38] This is primarily due to the fact that currently available AAV serotypes cannot reach the RPE following IVT administration.[38-40] The subretinal delivery requires creation of a fluid "bleb" between the photoreceptor and RPE, disrupting the interdigitation of the photoreceptor outer segments and the RPE apical processes.[41] There have also been several cases of chorioretinal atrophy following subretinal delivery of Luxturna (voretigene neparvovec-rzyl; Spark Therapeutics), the first FDA approved gene therapy for an inherited retinal disease which uses an AAV2 vector delivering a functional copy of *RPE65* to treat RPE65-associated Leber congenital amaurosis.[42-48] Furthermore, the therapeutic reach of subretinal injection is spatially limited. The vector transduction has been shown to be confined primarily to the area of retinal detachment (the bleb) rather than achieving pan retinal transduction.[49,50] Lastly, the complexity of subretinal surgery necessitates general anesthesia and specialized vitreoretinal training for the surgeon.[38,51,52]

The alternative, less damaging surgical delivery method is intravitreal injection (IVT) where the needle remains within the vitreous, avoiding direct contact with the retina. This is an outpatient procedure that requires less training for the ocular surgeon.[25] Since the vector is delivered into the vitreous, this approach offers the potential for pan-retinal transduction, in contrast with the localized treatment area of a subretinal bleb.[40] However, a significant barrier to IVT efficacy of AAV delivery to the outer retina is the internal limiting membrane (ILM).[53] The AAV serotype 2 capsid, most used for retinal therapy, has a binding domain with high affinity for HSPGs.[54,55] HPSGs are heavily concentrated in the ILM, acting as a 'sink' that sequesters viral particles and prevents their migration into the outer retina.[9,53,56]

1.4.2 AAV2 Capsid Based Library Synthesis for High-Throughput Screening Method

Binding property differences, or tropism differences, of various AAV serotypes have been a limitation in several early studies of AAV transduction for other tissues. AAV1 and AAV6 have been proven to show better tropism for muscle tissue compared to AAV2.[57] Scientists began to utilize advantageous structural regions of different capsids and combine them to create hybrid capsids. In this way, creating a hybrid capsid of AAV2 with selected AAV1 domains had been proven to increase the capsid's tropism for muscle.[58] However, it is important to note that making structural changes to a capsid can also negatively affect several other aspects like packaging capability, timing of transgene expression, and intracellular trafficking.[59,60] AAV capsids have a history of inducing immune responses in animal models and patients, especially when higher doses, or viral titers, are used, which can have harmful effects.[5,61,62] Optimizing an AAV capsid for therapeutic treatment is a complex process and involves lengthy *in vivo* testing for efficacy. Additionally, safety profiling is necessary before any capsid is used in a clinical setting.

There is preserved homology between AAV serotypes' structures, however, variable regions I-IX are defined as outer surface loops that differ between serotypes responsible for cell surface receptor, AAVR, interaction which AAVs rely on for cell entry. Due to variability within loops I-IX, each serotype interacts with AAVR a little differently.[8] While the nature of the transduction and binding properties are not entirely characterized, AAV serotype 2 has been shown to have tropism to the highest number of retinal cells overall compared to other serotypes.[63,64] This does not necessarily correlate to AAV2 being the best serotype for retinal delivery. AAV5, AAV8 and AAV9 are all being explored in the retinal therapy space due to high photoreceptor tropism with a subretinal delivery.[53,65] However, AAV2 surpasses other serotypes in RPE tropism, putting a significant number of inherited retinal dystrophies in line for therapeutic development with this. Here, there is a balance between all aspects needed to create a capsid capable of reduced ILM binding, but maintained or enhanced cell-specific tropism.

One strategy for cell-specific targeting or optimized transduction of AAV capsids is conducting a high-throughput screening of capsid libraries. AAV2, proven to have better transduction results within the retina, has been used in various capsid modification studies. In successful efforts to reduce neutralizing antibody binding, polyethylene glycol (PEG) chains have been added to AAV2 while maintaining transduction efficiency. PEG is additionally advantageous due to its non-immunogenic and non-toxic properties.[66] An alternative method, using biotinylation of the AAV, has increased cell surface binding and transduction efficiency dramatically. Biotin has a high affinity to streptavidin, so when a biotinylated AAV capsid is coupled with a streptavidin-EGF (epidermal growth factor) conjugate, there is enhanced binding of the capsid to cells with EGFR (EGF receptor) within the extracellular matrix.[7] These are just some examples of capsid structure engineering strategies that can enhance viral performance in different contexts.

Two individual studies separately identified a region of AAV2 that binds to HSPG: AA585 and AA588, which fall between or adjacent to loops IV and VII-IX.[9,67] Within these studies, researchers mutated these two specific arginine residues and tested the capsid on heparin-agarose. They proved that these sequence changes did not affect any other aspect of the capsid performance but successfully reduced heparin binding. Another study with the same goal, added an RGD motif to after AA587, creating an exposed loop on the outer surface of AAV2.[10] [68]Transduction efficiency dramatically increased for cells that AAV2 could not originally transduce. Although these many strategies were effective, all these engineered capsids did not surpass transduction patterns and overall coverage of wildtype AAV2.

Capsid engineering possibilities are not limitless. If too large a peptide is added to the capsid sequence within the VP1-3 region, the peptide can interfere with capsid synthesis. Across several studies, a peptide insertion between 6 to 10 amino acids (AAs) has been proven to produce the best results.[69-71] Moreover, AAs interact with each other, so it is essential to determine an optimal peptide sequence where neighboring AAs are not disrupting the overall capsid function desired. Many of these AA interactions are unpredictable before peptide formation and characterization.

In a notable study by Muller *et al.* 2003, the researchers set out to combat the HSPG binding of AAV2 and utilize all of the learned advantages and disadvantages in the above strategies to create a novel capsid.[69] With knowledge of the HSPG binding residues and the optimal length of peptide insertions necessary for proper capsid synthesis, Muller *et al.* created a library of AAV2 capsids with randomized 7-AA peptide insertions after AA587. The insertion is flanked by spacers on either side, glycine at the 5' end and alanine at the 3' end. This method was modeled after the phage display peptide library tool, which is an established method for discovering binding motifs, mostly performed with 7-mer or 12-mer peptides. Muller *et al.*'s peptide library strategically produced capsids that prevent arginine-arginine interactions on the outer surface of the capsid at the HSPG binding motif. Altering capsid tropism for cell targeted gene therapy has widely expanded because of this study.

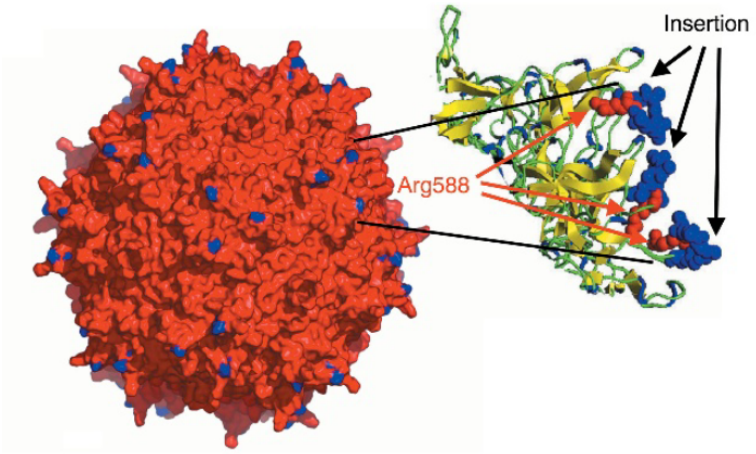

5' GGC CAG AGA GGC TTG CCT CAG GCT CGG TCT CAT GCC CAG GCG GCC 3'

G Q R G L P Q A R S H A Q A A

Figure 1.4.2.1 *Engineered AAV2 capsid variant from randomized 7-mer peptide library.* Pictured is a single variant from the randomized 7-AA peptide insertion library with an AAV2 capsid sequence based, adapted from the Muller *et al.* 2003 study. (Top) AAV2 capsid colored in red-orange with inserted, repeating outer surface loops colored in blue. Higher magnification of the HSPG binding motif region shows the insertion at the arginine residue AA588. (Bottom) DNA sequence of the insertion site shown in black. Red-orange AA sequences flank the blue AA sequence of a random 7-mer peptide insertion.

The full potential of capsid engineering for retinal gene therapy expands very far, particularly in the context of non-invasive delivery routes that could broaden both the therapeutic targets and the patient population who might benefit. A clinically meaningful question is whether a single structural modification to the AAV2 capsid surface is sufficient to overcome the ILM barrier and improve tropism toward the RPE from the vitreous. Building on the foundation described in this chapter, the work presented in this dissertation applies a similar approach to identify AAV2 capsid variants capable of overcoming the ILM barrier and achieving RPE transduction following IVT delivery.

Chapter 2 High-throughput screening of structurally variable AAV capsids yields a capsid capable of RPE transduction following intravitreal delivery

2.1 Introduction

With the largest limitation of RPE transduction following IVT delivery being anatomical barriers like HSPG binding, it would be most effective to structurally alter the AAV capsid surface to improve delivery efficiency. In the past, capsid engineering studies have been able to overcome this obstacle *in vitro*. Despite proven reduction to HSPG binding in heparin agarose models and even *in vivo* murine models, many studies have not been able to preserve wildtype transduction efficiency in the same capacity.[9,72,73]

Previously published AAV2-7mer library screening results, involving a directed evolution strategy, resulted in identification of a novel AAV2-based capsid, called 7m8, capable of photoreceptor transduction with IVT delivery in mice and NHP.[39] Directed evolution is a method that simulates natural selection within controlled parameters and rapid progression between stages. Using a capsid library and defined selection criteria, best-performing candidates are isolated and subject to iterative rounds of mutations and filtered selection. This can lead to identification of a capsid with desired properties, including enhanced cell-specific tropism, tissue migration, and safety.[74] With IVT injection, AAV2.7m8 was capable of posterior tissue migration and efficient transduction of inner and outer retinal neurons. Photoreceptor transduction was shown in this study[39], however, therapeutic applications with an IVT injection and PR transduction have not yet been accomplished. This study shows that capsid modifications for improved performance is a valuable tool for the future of disease treatment. Following this screening by Dalkara *et al.*, AAV2.7m8 became the benchmark AAV2-based capsid for retinal degenerative gene therapy.

Although, AAV2.7m8's transduction capacity is impressive and a large step forward in capsid delivery within the ocular disease context, RPE transduction with IVT delivery continues to be a gap in the field. To overcome this, we employed capsid engineering to alter the outer surface structure of AAV2, AAV4 and AAV5 and screened these capsids *in vivo*. Filtering for capsids with reduced HSPG binding and evident RPE transduction can bring us closer to an impactful vehicle for gene therapy. The development of a capsid capable of safe, efficient RPE transduction via IVT injection would dramatically improve the clinical treatment of inherited retinal diseases.

2.2 Results

2.2.1 AAV Library Screening in Mouse, NHP, and Canine for Novel Capsid Discovery

Utilizing the same AAV2-7mer library[39,72,75], we completed a high-throughput screening in mouse, NHP, and canine eyes to find an AAV2-based capsid capable of efficient RPE transduction following IVT administration in both mouse and a larger species, with the goal of identifying a variant with translational potential for human gene therapy. The AAV2-7mer library has a 10 AA (AA) string inserted between AA587 and AA588, which is known to interfere with the HSPG binding motif of the capsid.[34] The first 2 AAs are consistently Leucine and Alanine while the last AA is always Alanine. These 3 AAs tether the inserted loop to the outer surface of the AAV2 capsid. The true variable region is the 7 AA string between these linker residues. With 20 possible AAs at each of the 7 positions (20^7), the library possesses a theoretical diversity of $1.28x10^9$ unique variants. While the library was generated using standard triple transfection methods[10], the actual complexity of the packaged library used in this study was not empirically determined via deep sequencing. While previous studies utilizing similar production scales have reported library titers as high as 10^{13} viral genomes[36], the functional diversity (number of unique clones) is constrained by the transfection efficiency of the producer cells. We completed one round of *in vivo* screening in four mouse eyes and two macaque eyes to select variants with enhanced RPE tropism. The canine screening included 5 rounds of directed evolution to hone in one a top performing variant.

Figure 2.2.1.1A illustrates the recovery metrics from NHP RPE sections which exhibited a broad range of total recovered reads, varying from 11 to 9,880 per sample. In most sections, the population was dominated by a single top-performing variant, which accounted for 89.6-92.7% of total reads. This dominance was not observed in the nasal sections from both left and right eyes with 22 and 23 PCR cycles, respectively. The low read count for the nasal section from the right eye with 23 PCR cycles is likely due to loss of cell recovery during tissue processing.

Figure 2.2.1.1B presents the parallel screening results from the mouse eyes (N=4, P168 littermate males). In contrast to the robust recovery in NHPs, the mouse samples yielded significantly lower total read counts, ranging from 6 to 68 reads per eye. Lower read counts reflect biological differences in the number of total RPE transduction events compared to an NHP. Despite this limited recovery, the top-performing variants exhibited a similar pattern of dominance within the retrieved pool. However, the magnitude of this dominance (percent abundance of total reads) was lower than that observed in the NHP samples. This reduced convergence is likely attributable to the stochastic effects inherent in sampling such a small total number of recovered variants.

A

NHP						
Quadrant	Eye	PCR Cycles	Top Variant	# Reads of Top Variant	# of Total Recovered Reads	%
Superior	Right	22	LTHQDTTKNA	9163	9880	0.92742915
Superior	Right	23	LANQEHVKNA	8848	9563	0.92523267
Nasal	Right	21	QAHQDTTKNA	3152	3484	0.90470723
Nasal	Right	23	LANQEHVKNA	6	11	0.54545455
Temporal	Right	21	LANQEHVKNA	4773	5188	0.92000771
Temporal	Right	22	LALIQDSMRA	2240	2403	0.93216812
Temporal	Right	23	LANQEHVKNA	5203	5614	0.92679017
Inferior	Right	23	LTHQDTTKNA	5865	6345	0.92434988
Nasal	Left	22	LALIQDSMRA	698	1011	0.69040554
Temporal	Left	22	LAHQDTTKNA	6476	7226	0.89620814

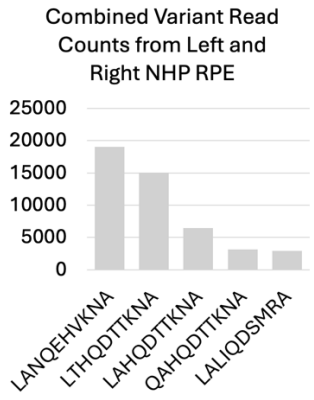

B

MURINE					
Mouse	Eye	Top Variant	# Reads of Top Variant	# of Total Recovered Reads	%
1	Right	LATKQPTSNA	10	13	76.92%
1	Left	LANQEHVKNA	31	68	45.59%
2	Right	LALPTQSDNA	6	9	66.67%
2	Left	LATKQPTSNA	5	6	83.33%

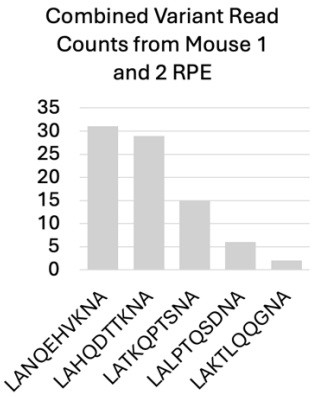

Figure 2.2.1.1. *Next-generation sequencing recovery metrics from mouse and NHP RPE DNA post-IVT injection of AAV2-7mer library* **(A)** NHP rectangular RPE sections divided by nasal, temporal, superior, inferior and left and right eyes. **(B)** Mouse eyes divided by individual mouse (1 or 2) and left and right eyes. Next-generation sequencing provides read counts of each variant ("# Reads of Top Variant"), ranked from highest to lowest. Percent of total occurrences of each top variant within # of total recovered reads for each sample is listed under "%."

Canine library screening data acquisition was conducted differently. The AAV2-7mer library underwent 5 rounds of injections in single eyes, with the alternate eye serving as an internal control. For each subsequent injection, or round, the extracted DNA from retinal tissue, inclusive of the RPE layer, was repackaged and cloned into plasmids for AAV production. By round 5, the performance of "LAHQDTTKNA" was enhanced drastically and highly outperformed the other capsid variants delivered. This variant was ranked as the third highest performing capsid from the NHP screening and second highest performing capsid from the mouse screening. Being the only

capsid that appeared in the NGS results for all three species, AAV2.LAHQDTTKNA was included to be further tested at a higher concentration in mice, driving expression of reporter gene, *GFP*. Surprisingly, shown in Figure 2.2.3.1., this capsid did not display preserved RPE transduction in mice. However, it is important to note that the only other variant between the top 4 further tested in mice that displayed RPE transduction was AAV2.LTHQDTTKNA which is only 1 AA different from AAV2.LAHQDTTKNA.

The directed evolution NGS metrics are displayed for reference in figure 2.2.1.2. Besides AAV2.LAHQDTTKNA, there is minimal overlap of top 5 ranked capsid variants in between rounds of screenings. AAV2.LAHQDTTKNA consistently remained the top performing capsid throughout each round, while "LAISDQTKHA" appears as top 2 in round 2 and top 3 in round 5, increasing in enrichment from 238 reads to 668 reads, respectively. "LAKANQNTPA" also increases in read number from round 1 to 3, peaking at top 3 by round 3 and then plunging in read number in subsequent rounds. There are multiple factors at play in what constitutes a top performing capsid variant besides retinal neuron layer migration and RPE cell surface binding. As stated in Chapter 1.4.2 and 2.3, the packaging ability differs across different capsids depending on the structure. While capsids are packaged at different concentration each round, some may outperform others resulting in a higher overall concentration in the final solution and ultimately stronger RPE transduction. It is possible that AAV2.LAHQDTTKNA has a high packaging score alongside its ability to traverse the retina and bind to RPE cells. Despite this capsid's dramatic increase in performance in canines, it only appears as the top performing capsid within the temporal region of the left eye in NHP, while AAV2.LTHQDTTKNA surpasses AAV2.LAHQDTTKNA in the NHP final ranking. Due to the almost identical structure of both capsids, it is possible that there is competitive inhibition of LAHQDTTKNA in the NHP screening, however, this was not tested.

CANINE				
Round	Top Variant	# Reads of Top Variant	# of Total Recovered Reads	%
1	LAHQDTTKNA	311	2832	10.98%
	LASSPTTKSA	263	2832	9.29%
	LASPKTASNA	255	2832	9.00%
	LALGRGADGA	189	2832	6.67%
	LAKANQNTPA	173	2832	6.11%
2	LAHQDTTKNA	327	2278	14.35%
	LAISDQTKHA	238	2278	10.45%
	LAGAKAQVPA	228	2278	10.01%
	LAKANQNTPA	199	2278	8.74%
	LAKQAPEKSA	195	2278	8.56%
3	LAHQDTTKNA	3096	6847	45.22%
	LANQDYTKTA	626	6847	9.14%
	LAKANQNTPA	392	6847	5.73%
	LAGAKAQVPA	287	6847	4.19%
	LAASDSTKAA	279	6847	4.07%
4	LAHQDTTKNA	14968	18949	78.99%
	LAKSDQSKPA	690	18949	3.64%
	LAKQQSASTA	476	18949	2.51%
	LAASDSTKAA	291	18949	1.54%
	LAVDGAQRSA	279	18949	1.47%
5	LAHQDTTKNA	21967	28905	76.00%
	LAKSDQSKPA	871	28905	3.01%
	LAISDQTKHA	668	28905	2.31%
	LAPDSTTRSA	455	28905	1.57%
	LAKQQSASTA	414	28905	1.43%

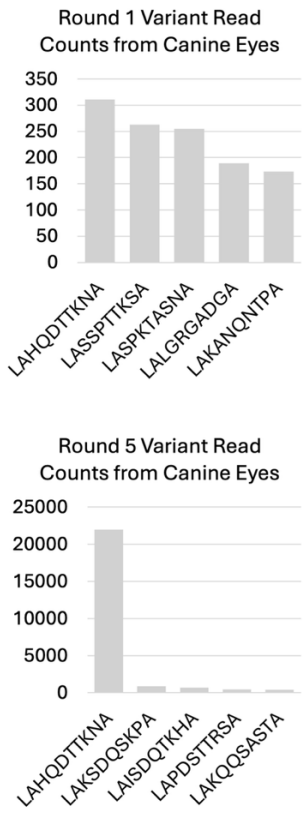

Figure 2.2.1.2. *Next-generation sequencing recovery metrics from canine RPE DNA after 5 rounds of IVT injection of AAV2-7mer library* Next-generation sequencing provides read counts of each variant ("# Reads of Top Variant"), ranked from highest to lowest. After 5 rounds of directed evolution of AAV2-7mer library injected canine eyes, the top performing variant was LAHQDTTKNA, displayed in the bar plot. Each subsequent round shows increasing read numbers for this variant as selection progressed. Percent of total occurrences of each top variant within # of total recovered reads for each sample is listed under "%."

2.2.2 Alternative AAV Library Screenings in Mouse

In addition to the AAV2-7mer library, alternative sequence changes of VP3 were made to create two more AAV2-based libraries. The AAV2.LoopSwap588 library does not have any peptide insertions, but instead three outer surface loops are altered. Within the AA sequence, every combination of monomers is assembled at AA585-589, AA591-594, and AA597 to generate a library. With more variable AA positions compared to the AAV2-7mer library, the theoretical diversity of AAV2.LoopSwap588 is 2.05×10^{13} variants.

Variant	1	2	3	4	5	6	7	8	9	10	11	12	13
ORF AA position	585	586	587	588	589	590	591	592	593	594	595	596	597
ORF – AA	R	G	N	R	Q	A	A	T	A	D	V	N	T
ORF – Codon													
A	A	A	A	A	A	A	A	A	A	A			A
C	C	C	C	C	C		C	C	C	C			C
D	D	D	D	D	D		D	D	D	D			D
E	E	E	E	E	E		E	E	E	E			E
F	F	F	F	F	F		F	F	F	F			F
G	G	G	G	G	G		G	G	G	G			G
H	H	H	H	H	H		H	H	H	H			H
I	I	I	I	I	I		I	I	I	I			I
K	K	K	K	K	K		K	K	K	K			K
L	L	L	L	L	L		L	L	L	L			L
M	M	M	M	M	M		M	M	M	M			M
N	N	N	N	N	N		N	N	N	N		N	N
P	P	P	P	P	P	P	P	P	P	P			P
Q	Q	Q	Q	Q	Q		Q	Q	Q	Q			Q
R	R	R	R	R	R		R	R	R	R			R
S	S	S	S	S	S		S	S	S	S			S
T	T	T	T	T	T		T	T	T	T			T
V	V	V	V	V	V		V	V	V	V	V		V
W	W	W	W	W	W		W	W	W	W			W
Y	Y	Y	Y	Y	Y		Y	Y	Y	Y			Y
Variant AAs	20	20	20	20	20	2	20	20	20	20	1	1	20

Figure 2.2.2.1 *AAV2.LoopSwap588 library design template.* Every AA possibility is listed below the AA position within VP3 of a wildtype AAV2 capsid.

With the same concept of loop altering, the AAV2.LoopSwap453 library contained combinations of monomers at AA446-447, AA449-451, and AA454-459, with a theoretical diversity of 4.1 x 10^{14} variants.

Variant	1	2	3	4	5	6	7	8	9	10	11	12	13	14
ORF AA position	446	447	448	449	450	451	452	453	454	455	456	457	458	459
ORF – AA	S	R	T	N	T	P	S	G	T	T	T	Q	S	R
ORF – Codon														
A	A	A		A	A	A			A	A	A	A	A	A
C	C	C		C	C	C			C	C	C	C	C	C
D	D	D		D	D	D			D	D	D	D	D	D
E	E	E		E	E	E			E	E	E	E	E	E
F	F	F		F	F	F			F	F	F	F	F	F
G	G	G		G	G	G	G	G	G	G	G	G	G	G
H	H	H		H	H	H			H	H	H	H	H	H
I	I	I		I	I	I			I	I	I	I	I	I
K	K	K		K	K	K			K	K	K	K	K	K
L	L	L		L	L	L			L	L	L	L	L	L
M	M	M		M	M	M			M	M	M	M	M	M
N	N	N		N	N	N			N	N	N	N	N	N
P	P	P		P	P	P			P	P	P	P	P	P
Q	Q	Q		Q	Q	Q			Q	Q	Q	Q	Q	Q
R	R	R		R	R	R			R	R	R	R	R	R
S	S	S		S	S	S	S		S	S	S	S	S	S
T	T	T	T	T	T	T			T	T	T	T	T	T
V	V	V		V	V	V			V	V	V	V	V	V
W	W	W		W	W	W			W	W	W	W	W	W
Y	Y	Y		Y	Y	Y			Y	Y	Y	Y	Y	Y
Variant AAs	20	20	1	20	20	20	2	1	20	20	20	20	20	20

Figure 2.2.2.2 *AAV2.LoopSwap453 library design template.* Every AA possibility is listed below the AA position within VP3 of a wildtype AAV2 capsid.

The residues altered in the AAV2.LoopSwap588 library encompass the HSPG binding motif of the capsid. This approach is an alternative method to reducing HSPG binding of AAV2 but preserving the existing AA content of the capsid rather than adding an outer surface loop, like with the AAV2-7mer library.

Some advantages are present with other AAV serotypes like AAV4, AAV5 and AAV8 which can withstand neutralization of antibodies better than AAV1-6. In addition, AAV4 and AAV5 utilize a different mechanism than AAV2 for cell surface binding.[76] These two serotypes require sialic acid binding for cell transduction and their cell surface structure homology with AAV2 is only 60%.[77] In fact, they both do not bind HSPG entirely but have high tropism to retinal cells.[78] It has been shown previously that if HSPG binding is induced in AAV5, then it generates high affinity to HSPG and does not demonstrate the same level of neutralizing antibodies, while maintaining a high packaging titer.[79] Finally, several studies have tested overall retinal tropism of both AAV4 and AAV5. One particular study created a recombinant AAV, where AAV2 and AAV4 were combined to create a hybrid capsid, which increased tropism for RPE cells in rat, dog, and NHP following a subretinal delivery.[80] Another study similarly combined AAV2 and AAV5, resulting in 70% RPE cell transduction in mouse embryonic stem cell-derived RPE compared to all other AAVs tested, like AAV2/8, AAV2/8, and ShH10 (derived from AAV6 for Müller glia selectivity).[81] For these capsid performance reasons, libraries were generated using an AAV4 and AAV5 backbone where a peptide insertion was added within VP3. The insertion sites of the peptide sequence and the length of the linkers differed between each 7mer library. The AAV4-7mer library insertion was at AA586 and the AAV5-7mer library insertion was at AA576 with "TG" and "GLS" as the upstream and downstream linkers, respectively, for both libraries. The theoretical diversity remained the same for all 7-mer libraries as the number of variable AAs remained as seven.

Variant	1	2	3	4	5	6	7	8	9	10	11	12	13	14
ORF AA position	585	X	X	X	X	X	X	X	X	X	X	X	X	586
AA	N	T	G								G	L	S	S
wt														
A				A	A	A	A	A	A	A				
C				C	C	C	C	C	C	C				
D				D	D	D	D	D	D	D				
E				E	E	E	E	E	E	E				
F				F	F	F	F	F	F	F				
G			G	G	G	G	G	G	G	G	G			
H				H	H	H	H	H	H	H				
I				I	I	I	I	I	I	I				
K				K	K	K	K	K	K	K				
L				L	L	L	L	L	L	L		L		
M				M	M	M	M	M	M	M				
N	N			N	N	N	N	N	N	N				
P				P	P	P	P	P	P	P				
Q				Q	Q	Q	Q	Q	Q	Q				
R				R	R	R	R	R	R	R				
S				S	S	S	S	S	S	S			S	S
T		T		T	T	T	T	T	T	T				
V				V	V	V	V	V	V	V				
W				W	W	W	W	W	W	W				
Y				Y	Y	Y	Y	Y	Y	Y				
Variant AAs	1	1	1	20	20	20	20	20	20	20	1	1	1	1

Figure 2.2.2.3 *AAV4-7mer library design template.* Every AA possibility is listed below the AA position within VP3 of a wildtype AAV2 capsid.

Variant	1	2	3	4	5	6	7	8	9	10	11	12	13	14
ORF AA position	575	X	X	X	X	X	X	X	X	X	X	X	X	576
AA	S	T	G								G	L	S	S
wt														
A				A	A	A	A	A	A	A				
C				C	C	C	C	C	C	C				
D				D	D	D	D	D	D	D				
E				E	E	E	E	E	E	E				
F				F	F	F	F	F	F	F				
G				G	G	G	G	G	G	G	G			
H				H	H	H	H	H	H	H				
I				I	I	I	I	I	I	I				
K				K	K	K	K	K	K	K				
L				L	L	L	L	L	L	L		L		
M				M	M	M	M	M	M	M				
N				N	N	N	N	N	N	N				
P				P	P	P	P	P	P	P				
Q				Q	Q	Q	Q	Q	Q	Q				
R				R	R	R	R	R	R	R				
S	S			S	S	S	S	S	S	S			S	S
T		T		T	T	T	T	T	T	T				
V				V	V	V	V	V	V	V				
W				W	W	W	W	W	W	W				
Y				Y	Y	Y	Y	Y	Y	Y				
Variant AAs	1	1	1	20	20	20	20	20	20	20	1	1	1	1

Figure 2.2.2.4 *AAV5-7mer library design template.* Every AA possibility is listed below the AA position within VP3 of a wildtype AAV2 capsid.

All four additional libraries were intravitreally injected and analyzed after 3 weeks for RPE transduction. From the extracted DNA from RPE tissue of injected eyes, the only other libraries that were recovered with PCR amplification were AAV2.LoopSwap453 (AAV2.LS453) and AAV2.LoopSwap588 (AAV2.LS588), where the intensity of the DNA bands appeared higher than that of the AAV2-7mer library (Figure 2.2.2.5).

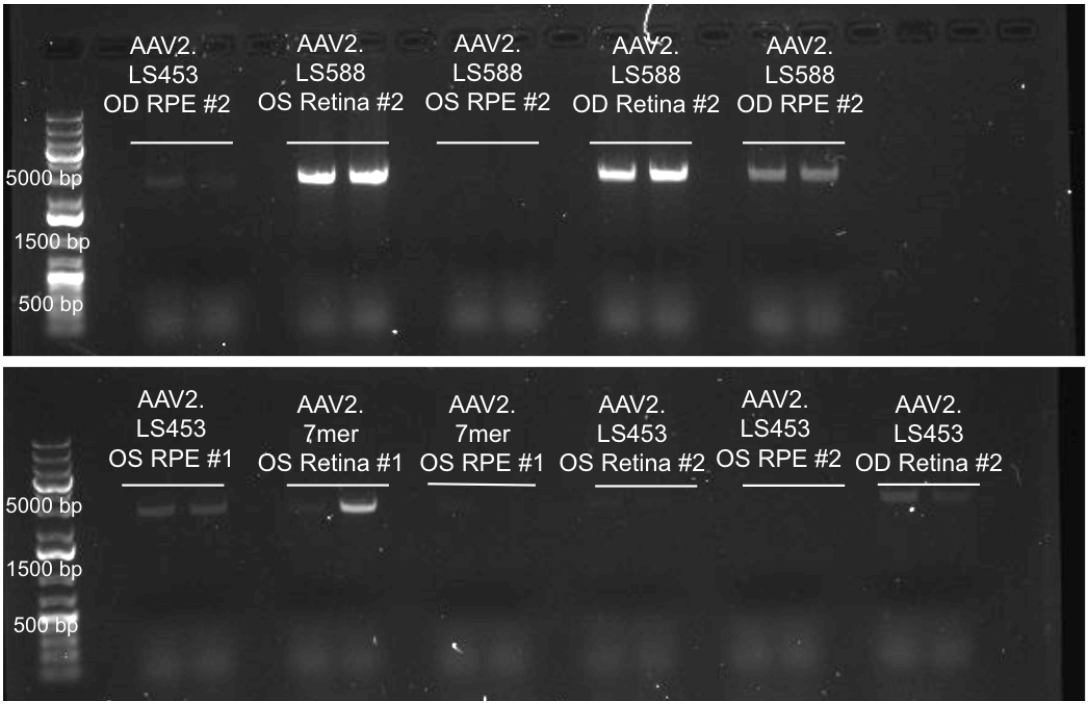

Figure 2.2.2.5 *AAV library PCR amplification and gel electrophoresis of DNA extracted from RPE cells of injected mouse eyes.* With primers amplifying the capsid sequence of all the libraries injected in the screening, only AAV2.LS453 OD RPE #2, AAV2.LS588 OD RPE #2, and AAV2.LS453 OS RPE #1 showed capsid amplification. AAV2.7mer is used as a positive control group.

Subsequent next-generation sequencing was performed to visualize AA sequences of the recovered capsid variants within the RPE tissue. Sequences were ranked by read count like the AAV2-7mer library screening. Due to more consistent recovery of capsid variants within the RPE layer following AAV2.LS453 injections, the top 4 ranked variants were re-packaged individually for further analysis. However, following packaging with *CAG-GFP* there was no GFP+ RPE identified in any of the injected mouse eyes (N=4, per vector; data not shown). With low evidence of this loop swap library transducing RPE cells with an IVT injection, we chose not to move forward with testing the AAV2.LS588 library and proceed with the successful candidates from the AAV2-7mer library screening.

MURINE					
Mouse	Eye	Top Variant	# Reads of Top Variant	# of Total Recovered Reads	%
1	Right	SNTNFFGGD	57	89	64.04%
1	Left	SETSNRGGH	3	22	13.64%
2	Right	SHTLWSSGHI	36	85	42.35%
2	Left	RRTKTTSGKT	1	12	8.33%

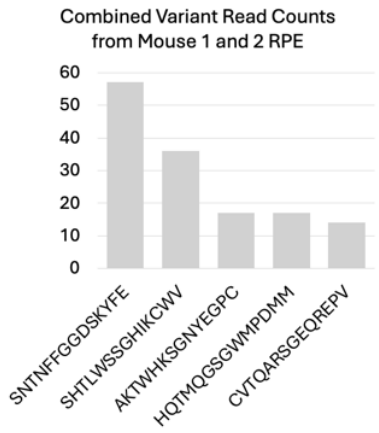

Figure 2.2.2.6 *Next-generation sequencing recovery metrics from mouse RPE DNA post-IVT injection of AAV2.LS453 library.* Mouse eyes divided by individual mouse (1 or 2) and left and right eyes. Next-generation sequencing provides read counts of each variant ("# Reads of Top Variant"), ranked from highest to lowest. Percent of total occurrences of each top variant within # of total recovered reads for each sample is listed under "%."

2.2.3 Candidate Selection and Functional Validation Strategy of Variant 3

To identify the most robust vectors, we cross-referenced the next-generation (NGS) datasets from the NHP and mouse screenings. Our analysis revealed a striking overlap in the highest-ranking variant between species. The top-performing candidate, with the insertion LANQEHVKNA, was consistent across both models, yielding 19,051 reads in NHP samples and 31 reads in mouse samples, where there is an exponential decrease in reads for each subsequent variant in the ranking. Based on these rankings, we selected four lead candidates for functional validation. These included the consensus top performer and three additional high-ranking variants: LANQEHVKNA (top performer, shared candidate between NHP and mouse), LAHQDTTKNA (shared candidate between all species), LATKQPTSNA (top 3 from mouse screening), and LTHQDTTKNA (top 2 from NHP screening, with one AA difference from top candidate from canine screening).

To evaluate the transduction profiles of these capsids, each variant was packaged with a GFP reporter gene driven by either the ubiquitous *CAG* promoter or the RPE-specific *BEST1* promoter. Equal numbers of male and female mice (n = 4-12 per group, P60-88) received IVT injections of these candidate vectors. Following a 3-week expression period, eyes were enucleated and processed as RPE flat mounts to quantify the percentage of GFP+ cells. We designated the top-performing peptide candidate, LANQEHVKNA, as Variant 3 (AAV2.Var3). The additional three high-ranking variants were evaluated (Figure 2.2.3.1), however, all displayed very poor retinal transduction. Only LTHQDTTKNA-*CAG-GFP* resulted in some peripheral RPE transduction, an unexpected result since this variant did not appear in the mouse screening results; however, LTHQDTTKNA was the second highest ranked variant from the primate screening. After conducting qualitative analyses across all injected eyes using fluorescence microscopy, <10 GFP+ RPE cells were observed in all samples injected with AAV2.LATKQPTSNA and AAV2.LAHQDTTKNA. Overall, AAV2.LTHQDTTKNA displayed GFP+ RPE cells at around 50% compared to that of AAV2.Var3, proving that AAV2.Var3 remained the top performing candidate. To evaluate AAV2.Var3's specific tropism for the outer retina, we compared its transduction profile against AAV2.7m8, a capsid known to transduce photoreceptors via IVT delivery but with minimal to no efficacy in the RPE, especially in primate.[39]

Vector	Titer
AAV2.LAHQDTTKNA-*CAG-GFP*	5.06 x 10^{14} vg/mL (1.012 x 10^{12} vg per eye)
AAV2.LATKQPTSNA-*CAG-GFP*	3.18 x 10^{14} vg/mL (6.36 x 10^{11} vg per eye)
AAV2.LTHQDTTKNA-*CAG-GFP*	6.39 x 10^{14} vg/mL (1.278 x 10^{12} vg per eye)

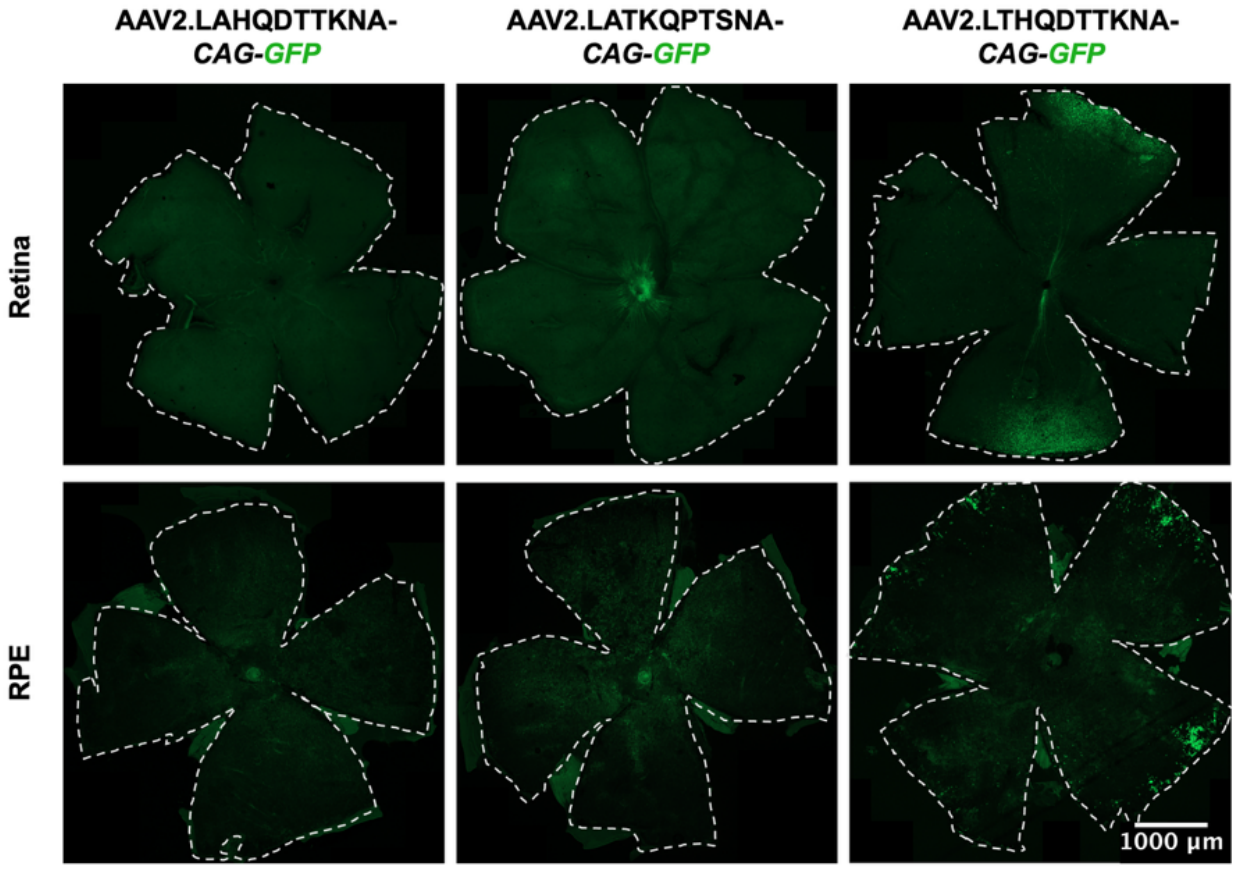

Figure 2.2.3.1 *Comparison of RPE transduction efficiency following IVT injection between high-ranking candidates: AAV2.LAHQDTTKNA, AAV2.LATKQPTSNA, and AAV2.LTHQDTTKNA* All capsids were packaged with *CAG* promoter driving expression of reporter gene, *GFP*. Injections of each vector were repeated in 4 mice (8 eyes) for GFP expression analysis. Flat mounts for each construct display poor GFP expression in retina and RPE tissue, compared to AAV2.Var3 (Figure 2.2.3.3).

A critical consideration in the clinical translation of AAV-based gene therapies is vector purity, as the presence of empty capsids, or those lacking nucleic acids, has been associated with increased immunogenicity and reduction of the efficacy of treatment.[82-84] Empty capsids retain the full antigenic surface of the AAV capsid and are capable of producing an immune response to the DNA-containing capsids, yet contribute no therapeutic benefit. An increased empty-to-full capsid ratio may reduce transduction efficiency by competing with full capsids for cellular entry and receptor binding.[85] To characterize the purity of our vector preparations prior to *in vivo* delivery, a mass photometry assay was performed on both AAV2.Var3-*CAG-GFP* (1.52×10^{14} vg/mL) and AAV2.Var3-*BEST1-GFP* (7.44×10^{14} vg/mL) stock solutions produced. Analysis of AAV2.Var3-*CAG-GFP* revealed that 92.8% of particles were full capsids, with only 7.2% empty and no ambiguous particles detected (N=1,283 particles). Similarly, AAV2.Var3-*BEST1-GFP* yielded 92.4%

full capsids and 7.6% empty (N=1,345 particles). These capsid numbers likely exceed those reported for some clinical-grade AAV preparations and indicate that the immunogenic and dose-associated risks with empty capsid contamination are minimal in the injection solutions used in this study.[82] A limitation with this experiment is a lack of AAV2.7m8 capsid data for comparison.

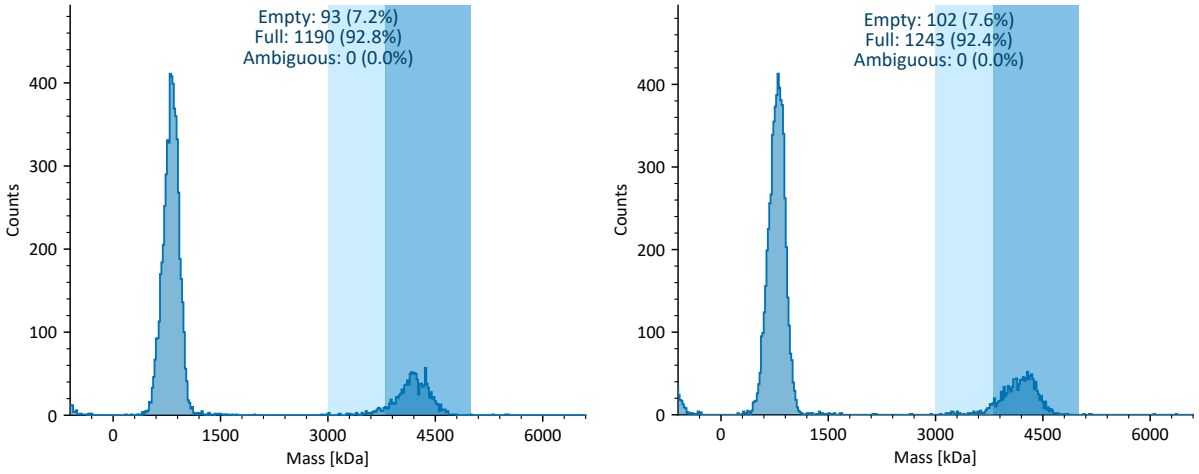

Figure 2.2.3.2 *Quantification of empty AAV capsids in injection-ready solution.* AAV2.Var3-*CAG-GFP* (right) and AAV2.Var3-*BEST1-GFP* (left) mass photometry data shows a very low empty-to-full capsid ratio. More than 92% of AAV capsids contain genetic material within the aliquot assayed in the figure. The dark blue region (3,800-5,000 kDa) includes all full capsids, while the light blue region (3,000-3,800 kDa) encompasses all empty capsids. The large peak around 750 kDa likely represents residual host cell proteins (HEK293).

Figure 2.2.3.3 presents representative retinal and RPE flat mounts (oriented with the injection site superior). As expected, retinal flat mounts demonstrated GFP expression for both vectors, confirming successful IVT delivery and inner retinal transduction. However, RPE flat mounts revealed a divergence in tropism. AAV2.Var3 mediated distinct GFP expression in the RPE, particularly in the periphery near the injection site, as well as in the ventral and temporal quadrants. In contrast, AAV2.7m8 failed to yield GFP expression in the RPE layer. High-magnification (20X) analysis confirmed these observations. Scanning of the AAV2.7m8 posterior eyecups exposing the RPE layer identified negligible transduction, limited to a single cluster of approximately 18 isolated GFP+ cells in the temporal-ventral region in the representative sample display and a range of 1-409 GFP+ cells for the entire treatment group overall. AAV2.Var3 induced RPE expression characterized by a "tiling" pattern, where large patches of neighboring cells expressed GFP. This phenotype was consistent across samples using both *CAG* promoter [3.04×10^{11} vector genomes (vg) delivered per eye] and *BEST1* promoter (1.49×10^{12} vg delivered per eye). Peripheral RPE transduction was detected in every injected sample driven by both promoter types.

Cross-sectional analysis of each retina including the RPE layer further elucidated each vector's transduction profiles (Figure 2.2.3.3). AAV2.7m8 transduced the ganglion cell layer (GCL) and inner nuclear layer (INL) with IVT injection, but no RPE cells. AAV2.Var3 displayed poor GCL and moderate INL transduction with IVT injection, but strong RPE transduction. Phalloidin was used as a counterstain to label actin filaments. AAV2.Var3-injected eyes displayed a reduction in phalloidin around the external limiting membrane (ELM).

The last row in Figure 2.2.3.3A displays a subretinal injection of AAV2.Var3 with *CAG* promoter driving expression of GFP. Here there is widespread GFP expression in the central, mid-periphery, and periphery of the dorsal, nasal, and temporal quadrants of the mouse eye. Cross-sectional analysis of the retina following subretinal injection shows GFP expression in more retinal neurons than with the IVT injection. GCL, amacrine cells, horizontal cells, and photoreceptor all display strong GFP expression. Figure 2.2.3.3B quantifies these findings of GFP expression in RPE cells, demonstrating higher expression in AAV2.Var3-injected eyes.

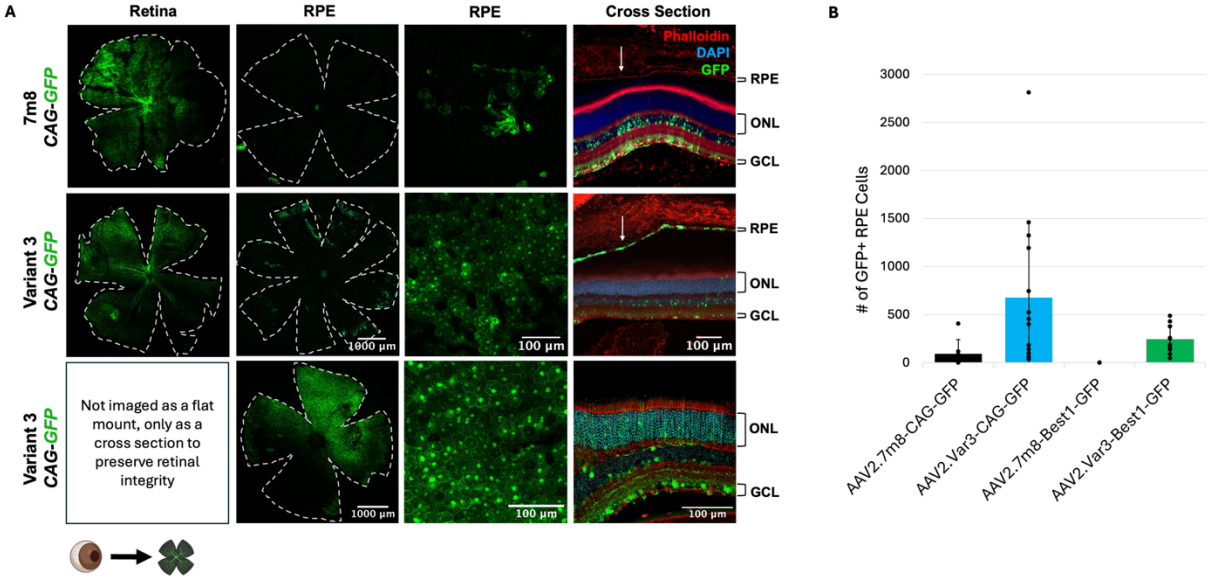

Figure 2.2.3.3 *Comparison of RPE transduction efficiency following IVT injection between AAV2.Var3-CAG-GFP and AAV2.7m8-CAG-GFP, including subretinal delivery of AAV2.Var3-CAG-GFP* **(A)** Top row: AAV2.7m8-*CAG-GFP*, IVT injection; Middle row: AAV2.Var3-CAG-GFP, IVT injection; Bottom row: AAV2.Var3-*CAG-GFP*, subretinal injection; all imaged at 3 weeks post injection. Retinal and posterior eyecup flat mounts of left eyes show GFP expression in retinal neurons and RPE. A zoomed in image of posterior eyecup flat mount shows GFP expression in individual RPE cells. Separation of retina from posterior eyecup is a histological artifact of enucleation and dissection, but retina remained attached at the optic nerve and ora serrata. **(B)** AAV2.Var3-*CAG-GFP* (N=14) shows a 7-fold increase in the average number of RPE cells per eye with GFP expression compared to AAV2.7m8-*CAG-GFP* (N=7). AAV2.Var3-*BEST1-GFP* (N=10) shows increased expression

compared to AAV2.7m8-*BEST1-GFP* (N=3) but a much lower average number than AAV2.Var3-*CAG-GFP* despite a comparable range of titers. Data shown as mean (SD).

2.2.4 Translational Validation of RPE Transduction of Variant 3 in NHP Eye

To test the clinical translatability of our vector to primates, we administrated Variant 3 packaged with the RPE-specific promoter, *BEST1*, driving expression of reporter gene, *GFP*, to the NHP *Macaca mulatta* (rhesus macaque). The NHP right eye and left eye were injected on the same day. The right eye was injected with 150 μL of 3.5 x 10^{13} vg/mL (5.8 x 10^{12} vg). The left eye was injected with 150 μL containing 43 μL of 3.5 x 10^{13} vg/mL (1.5 x 10^{12} vg) and 107 μL of Balanced Salt Solution. A predicted 130-135 μL volume likely entered the eyes during the procedure. The NHP received intramuscular steroid injections starting 3 days prior to the AAV injection and continued until eye inflammation went down. Color fundus, red-free fundus, fluorescein angiography, fundus autofluorescence, spectral domain optical coherence tomography (SD-OCT) and photopic electroretinograms did not show any signs of toxicity and abnormalities one week and twelve weeks after injections (Figure 2.2.4.1).

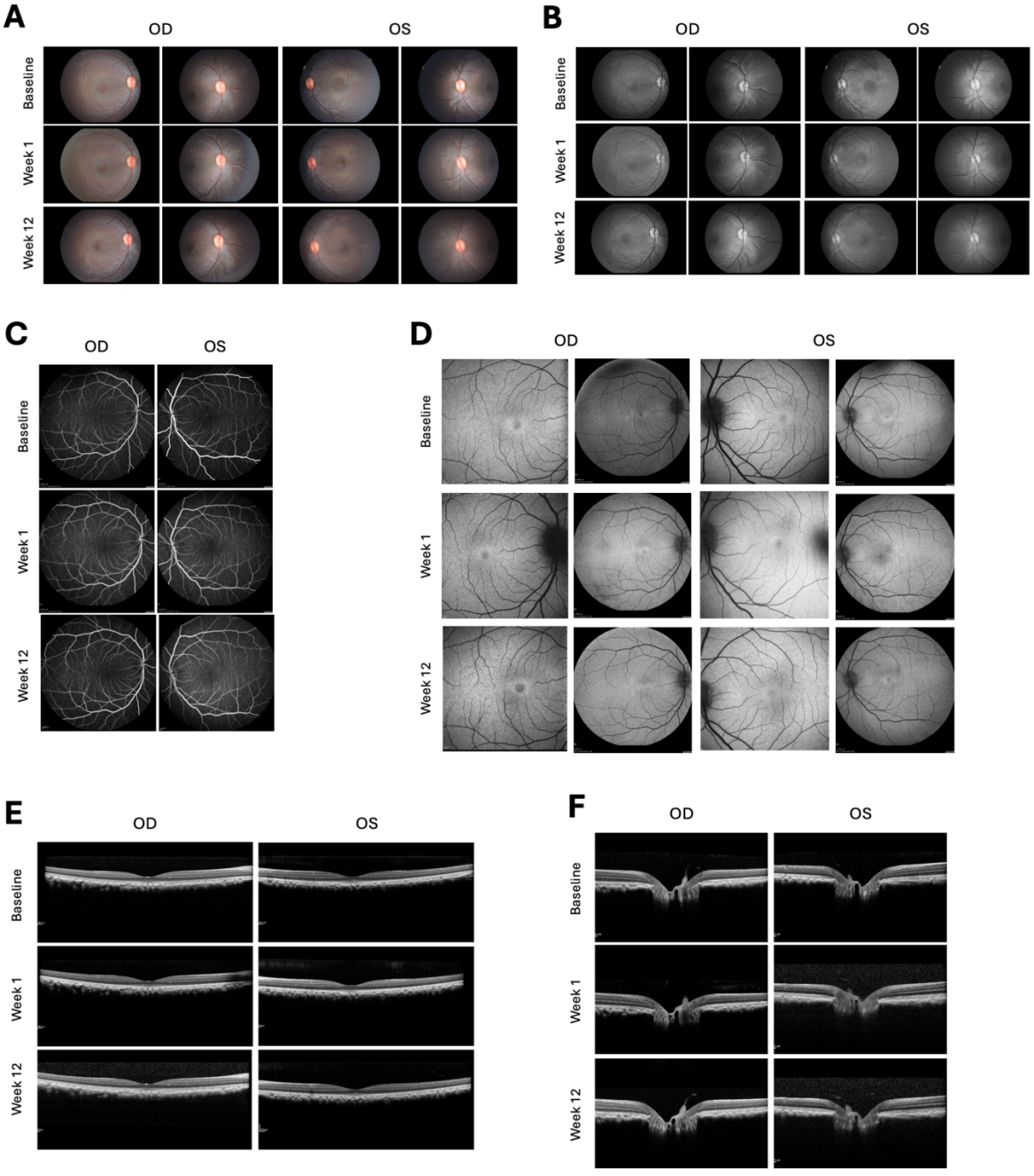
A
OD
OS
Baseline
Week 1
Week 12
B
OD
OS
Baseline
Week 1
Week 12
C
OD
OS
Baseline
Week 1
Week 12
D
OD
OS
Baseline
Week 1
Week 12
E
OD
OS
Baseline
Week 1
Week 12
F
OD
OS
Baseline
Week 1
Week 12

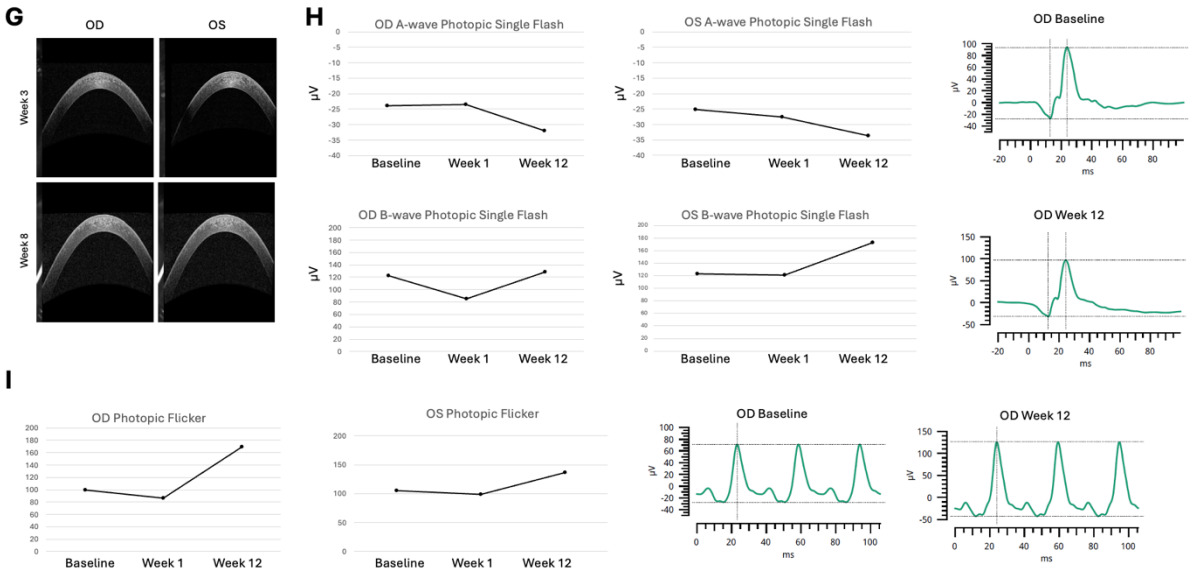

Figure 2.2.4.1 *Rhesus macaque injected with AAV2.Var3-BEST1-GFP in both eyes did not exhibit clinical signs of retinal toxicity or ocular inflammation* The color (**A**) and red-free fundus images (**B**) show normal anatomy of the macula and arcade vessels without exudation and no optic nerve swelling. Fluorescein angiography showed normal retinal vasculature without leakage. SD-OCT imaging of the macula (**E**) and optic nerve (**F**) showed normal foveal contour without cystoid macular edema and no optic nerve edema. Anterior segment OCT (**G**) showed normal cornea without edema without debris in the aqueous humor. Photopic full field ERG using single flash (**H**) and flicker (**I**) were within normal range at all timepoints.

Three months post-injection of AAV2.Var3-*BEST1-GFP*, both eyes were enucleated and fixed for imaging of the RPE cells. Each retina was separated into 4 quadrants: dorsal, nasal, temporal, and ventral. The macula region was also separated out for analysis. The right eye showed the most GFP+ RPE cells with very high expression in the periphery for all 4 quadrants (2448.91 x 2448.91 μm image of dorsal periphery shown, Figure 2.2.4.2A). Another peripheral region on the nasal quadrant is shown (Figure 3F and G, 2448.91 x 2448.91 μm and 319.45 x 319.45 μm regions). Mid peripheral regions also showed many GFP+ RPE cells with the number of GFP+ cells decreasing closer to the central retina, where the nasal mid periphery is shown (Figure 2.2.4.2C and D, 2448.91 x 2448.91 μm and 319.45 x 319.45 μm regions). The macula did not show any GFP, shown in a 2448.91 x 2448.91 μm region (Figure 2.2.4.2E). The left eye had significantly less GFP+ RPE cells with only low expression seen in the dorsal periphery. All other regions, including the macula, did not have visible expression of GFP in the RPE. One limitation in this experiment was that quantitative analysis of NHP RPE using our manual cell counting method was not conducted. However, qualitative analysis and intensity density comparison between nine equally distributed, 319.45 x 319.45 μm subregions with symmetrical eccentricities of the right eye was conducted and revealed an estimated 10-20% RPE transduction rate. The subregions included one at the macula,

four at the periphery of each quadrant, and four at the mid periphery of each quadrant. Overall, transduction patterns of AAV2.Var3 are similar in mouse and NHP, giving this novel capsid high translatability.

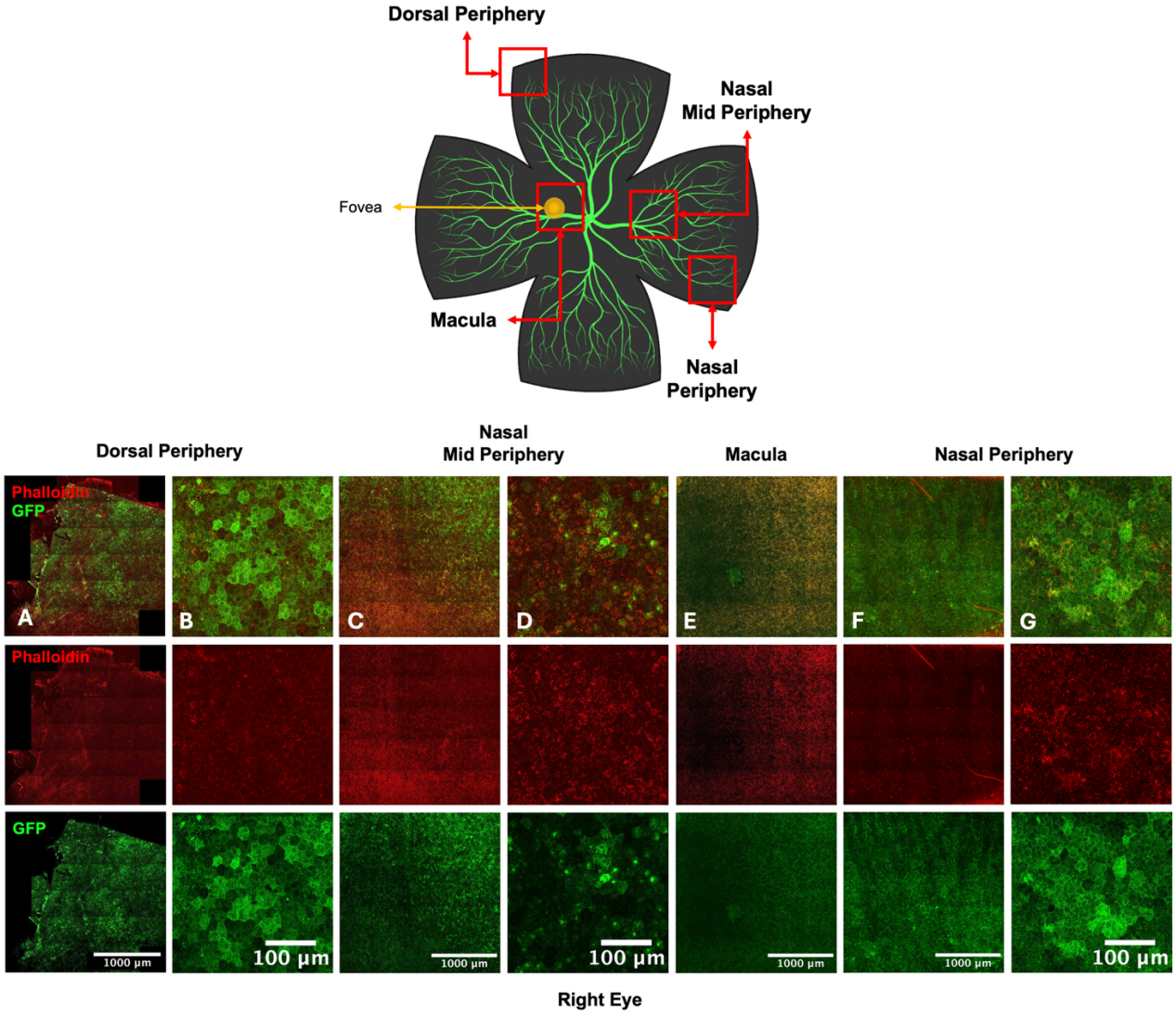

Figure 2.2.4.2 *Peripheral and mid peripheral GFP expression in high titer AAV2.Var3-BEST1-GFP delivery in right NHP eye* ***(A-D, F-G)*** Dorsal periphery, nasal mid periphery, and nasal periphery show high levels of GFP expression in RPE cells. Counter-stain with phalloidin is used to negate auto-fluorescence. **(E)** Macular region of the right eye does not show any GFP+ RPE. The flat mount diagram (top) displays the localization of the images acquired.

2.3 Discussion

Intravitreal injection has historically failed to efficiently target the RPE. The ILM acts as a physical barrier, trapping naturally occurring AAV serotypes via high-affinity interactions with HSPGs, particularly for AAV2, which is the backbone of most clinical retinal vectors. In this chapter, we show that structural modifications of the AAV2 capsid surface can overcome these barriers in both mouse and NHP.

In Kern *et al.* 2003, scientists tested several AAV2-based mutant capsids and analyzed infectivity, packaging, and binding of each. Capsids that encompassed mutations within the same residues altered in AAV2.LoopSwap453 (mutant #10 and #11) had a low ratio of the number of capsids to the number of infectious particles, giving it a good infectivity score, a low ratio of capsids to viral genomes, giving it a great packaging score, and lastly, more than 80% binding to HeLa cells and a heparin-agarose column.[67] Studies have shown that residues altered within this library (AA440-458) interact with other outer surface loops to increase stability for capsid packaging. Lastly, mutations between 448-451, 454 have been shown to reduce HSPG binding, making induced variability within these regions a strategy for achieving enhanced capsid transduction.[1] However, the loop swap libraries and AAV4/AAV5 libraries were unsuccessful in RPE transduction. This could have been partially due to no NHP data acquired for comparison. Without identifying variants that were conserved in RPE tropism between species, there is less likelihood for high performance from just one round of high-throughput screening. Instead, by inserting a 10-AA peptide to the outer surface of the AAV2 capsid at the HSPG binding locus (AA588), RPE transduction following IVT delivery was dramatically improved with AAV2.Var3 in mice and NHP. Within loop IV of VP3, AAs R585 and R588 interact and have high HSPG binding affinity.[9,56,67,86] Addition of the 7mer at AA588 prevents arginine binding. Also, the Variant 3 sequence "LANQEHVKNA" does not contain arginine and possesses a neutral charge and acidic properties. Such properties directly affect how the capsid binds to cell surface receptors and undergoes intracellular trafficking.[59,60] A lack of arginine on the AAV capsid has been proven in previous studies to reduce HSPG binding.[67] This design aligns with prior work showing that altering AAV2 HSPG binding can change retinal tropism and improve outer retinal penetration from the vitreous.

AAV2.Var3-*CAG-GFP* and AAV2.Var3-*BEST1-GFP* were IVT injected into mouse eyes and reached on average 10% of the total number of RPE cells in the mouse eye. Substantial similarity in NHP RPE transduction was seen, with a comparable level of expression within the epithelium. This level of RPE coverage is novel given that previously recorded RPE transduction from the vitreous has been negligible. This RPE transduction was achieved without mechanically detaching the retina from the RPE. One limitation regarding the overall assessment of the transduction patterns of these vectors and the other high-ranking vectors was a lack of a true control group, or an AAV capsid established to display no migration past the ILM or no RPE tropism. Including this data may have illuminated any potential false positive data, for example any accidental retinal detachments during the surgical procedure that may have allowed the capsids to reach the RPE cells more easily.

AAV2.Var3 consistently produced higher transduction and transgene expression in the peripheral retina compared to central regions in both mouse and NHP. This peripherally biased pattern is consistent with regions where the ILM is thinner, or the retinal periphery.[87] However, it is unclear why the same peripherally biased pattern is observed in mice, where the thickness of the ILM is more homogenous.[88] Additionally, there have been reports of increased ILM thickness in disease models, which could signify that the RPE transduction efficiency is reduced in *rd12* mice compared to initial AAV2.Var3 RPE transduction quantification assays with C57BL/6 mice.[89,90] Future work would be needed to determine whether modifying the injection parameters or capsid design can allow for better AAV migration across the ILM and improved RPE transduction closer to the macular region.

While we have not confirmed whether improved RPE transduction with AAV2.Var3 is a direct result of reduced heparan sulfate binding, our findings suggest that the peptide insertion likely disrupts the HSPG binding. Precise interactions can be elucidated using cryogenic electron microscopy. There is also a need for further analysis of the migration patterns seen with AAV2.Var3, like whether peripheral transduction is a result of different extracellular matrix cues in the periphery.

While library screenings and directed evolution studies have been conducted before, most efforts have focused on enhancing photoreceptor transduction. By conducting this screening in both mice and NHP, we were able to establish top-performing candidates shared between both species, which increases confidence in translational potential. This approach of extensive functional testing in the mouse model evades the scale and cost that would have been required to perform equivalent functional testing primarily in NHP. In conclusion, Variant 3 represents a significant step forward in vector engineering, offering a viable IVT platform for RPE-targeted gene therapy that achieves both barrier penetration and therapeutic efficacy while avoiding surgical damage and associated localized atrophy with a subretinal delivery.

2.4 Materials and Methods

2.4.1 AAV Library Generation

The combinatorial variant library (CVL) was constructed by Twist Bioscience. A sequence-verified clonal gene is used as a linear template which covers all constant regions of the library. Once verified, the template is amplified out of a prepared plasmid prior to construction. For the variable region, the template is split into multiple sections where oligo variants are designed for each section in pools of a few thousand each. Every oligo variant is explicitly designed at the DNA level to reflect the AA diversity requested. No degenerate synthesis is used to construct variable regions. The oligo variants from each section of the variable region are then combinatorially assembled using Twist

Bioscience's proprietary Seamless Assembly method, generating a variable domain of up to 10^{10}-10^{11} unique sequences (based on theoretical diversity of the design). Once constructed, the variable domain is assembled into the template at the specified position, amplified using a minimal number of PCR cycles, and verified by NGS. Plasmid backbone sequences were altered for improved ITRs, then packaged and purified at the University of California, Berkeley. Final titers of packaged libraries were 7.26 x 10^{14} vg/mL for AAV2-7mer, 3.52 x 10^{13} vg/mL for AAV4-7mer, 2.03 x 10^{12} vg/mL for AAV5-7mer, 5.4 x 10^{13} vg/mL for AAV2.LoopSwap453, and 7.9 x 10^{13} for AAV2.LoopSwap588.

2.4.2 AAV Intravitreal Injection

All animal procedures were approved by the Institutional Animal Care and Use Committee of the University of California, Berkeley or the University of California, Davis. All animal experiments were conducted in accordance with the ARVO Statement for the Use of Animals in Ophthalmic and Vision Research. All animal procedures also abide by all Arrive guidelines as stated: https://arriveguidelines.org.

Mice were intraperitoneally injected with a well-mixed combination of ketamine hydrochloride (100mg/kg) and xylazine (10mg/kg). When the mice were fully anesthetized, topical eye drops of 0.5% proparacaine, 1% tropicamide, and 2.5% phenylephrine were added to the surface of the eyes for 3 minutes each. To maintain lubrication of the cornea and to better visualize the target injection site, GenTeal Tears Lubricant Eye Ointment was applied generously to the surface of the eyes. Using a sharp 30-G needle, a hole was made at the dorsal pole of the eye right behind the ora serrata line. Immediately after, a blunt-ended 32-G Hamilton syringe was put through the hole to inject 1-2 μL of AAV2-7mer library in the vitreous space, ensuring not to nick the lens or stab the retina. Intraocular bleeding is a good indication that the retina has been stabbed. The Hamilton syringe was kept in the eye for 5 seconds after injection to reduce the amount of AAV that may flow back out of the hole. Tobramycin drops (Somerset Therapeutics LLC, NDC 70069-131-01) were added to the surface of the eye for 3 minutes following AAV IVT delivery. Soothe Lubricant Eye Ointment (Bausch + Lomb) was generously added to the surface of the eye until the mouse fully recovered and woke up from anesthesia. For all experiments, an equal distribution of female and male mice was used, unless otherwise stated.

One rhesus macaque (Macaca mulatta), one years old, was injected in both eyes through the IVT route. Both eyes received 150 μL of the AAV2.Var3-BEST1-GFP. The right eye and the left eye received 5.8x10^{12} and 1.5x10^{12} viral genomes, respectively. The AAV2.Var3-*BEST1-GFP* was injected undiluted in the right eye and diluted in BSS (Alcon, Fort Worth, TX, USA) in the left eye. Diluted and non-diluted AAV2.Var3-BEST1-GFP were loaded into a 0.5 mL low dead space Luer lock syringe (Air-Tite Products, Virginia Beach, VA, USA) using a 30G x1" BD PrecisionGlide needle (Becton, Dickinson and Company, Franklin Lakes, NJ, USA) and capped with a BD Syringe Tip Cap (Becton, Dickinson and Company, Franklin Lakes, NJ, USA). Low dead-space syringes

were used to optimize the volume that enters the vitreous space of the eye. Syringes were then stored on ice until injections. Prior injection, the animal was sedated with ketamine hydrochloride (5–30 mg/kg), midazolam (0.1 mg/kg), and dexmedetomidine (0.05–0.07515 mg/kg) intramuscularly and were medically monitored by a California National Primate Research Center (CNPRC) veterinarian and trained technician. While sedated and after eyes were dilated, the eyes were prepared and draped in the usual sterile fashion for ophthalmic surgery. An operating microscope was used in conjunction with a flat contact lens, two 25-gauge pars plana trocars placed superiorly, and a light pipe for visualization. While focusing on the macula, the needle was introduced through the second trocar and advanced near the macular surface and the virus was injected in the vitreous just above the macular surface. The trocars were removed, and topical antibiotic ointment was applied before the animal was taken to recover.

The rhesus macaque was born and kept at the CNPRC which is accredited by the Association for Assessment and Accreditation of Laboratory Animal Care (AAALAC) International. This study was approved by and performed according to the Institutional Animal Care and Use Committee (IACUC protocol #23774) of the University of California – Davis and the National Institutes of Health (NIH) Guide for the Care and Use of Laboratory Animals, respectively.

2.4.3 Next-Generation Sequencing for AAV2-7mer Library Screening

Two NHP eyes, 4 mouse eyes, and 5 canine eyes were injected with the AAV2-7mer library. For NHP and mouse this was a single-round, low-N exploratory screening where a reduced number of animals was used due to this being an early-stage experiment for candidate nomination. After IVT injection of the AAV2-7mer library, we waited 3 weeks in mice to evaluate DNA expression. Then, we enucleated all 4 eyes and extracted DNA from the posterior eyecup (RPE, choroid, sclera) for subsequent processing. NHP eyes were enucleated for analysis 17 days after injection. Twelve total rectangular sections of RPE were extracted from different quadrants of each eye, primarily the right eye. Only two sections were taken from the left eye (nasal and temporal). DNA was purified for NGS from each of the 12 NHP sections. For canines, this was a 5-round directed evolution screening where 1 eye was used each round in one dog, leaving the contralateral eye as an internal control.

We used primers to amplify just the capsid sequence of the AAV library and ran the amplified DNA on a gel to visualize the presence of the AAV library in our sample. If there was some amount of AAV library present (or a band was visualized), the band on the gel was extracted and purified. A much smaller 300 base pair region was amplified using PCR and then purified. NHP samples underwent a range of 21-23 PCR cycles. These smaller fragments of the AAV capsid region were inclusive of the variable region of the library. This DNA was submitted for NGS.

NGS data displayed the DNA sequence of each capsid variant amplified from the RPE of each sample and the read count which corresponds to the number of occurrences of each variant in the sample. A higher read count indicates a higher relative abundance of the variant from the isolated DNA. The AAV capsids were not replication competent, so PCR amplification allowed for detection of capsids within the RPE layer.

Using a python script, the 10-base pair sequence prefix of the 7mer variable region was located within each read allowing each subsequent 30-base pair region (the variable region) to be detected and quantified. Quantitatively ranked variants were outputted, listing the 30-base pair sequence and read count in order from highest to lowest. This represented the list of variants that most likely transduced RPE cells in the injected eyes, where higher read counts corresponded to more abundance of the variant within the sample. Several variants from the NHP and canine screening reoccurred within the list, so after calculating the read count totals for each variant, the list was consolidated and illustrated to include the top 50 performing variants in Figure 2.2.1.1. The top 50 performing variants were used for analysis and comparison overall for mouse and canine data as well, where the "# of Total Recovered Reads" reflects the data from this subset.

2.4.4 RPE Imaging and Cell Quantification

Each eyeball sample was dissected to remove the anterior half of the eyeball, lens, and vitreous. Then, 4 cuts were made towards the center to allow the eyecup to flatten using established flat mount procedures.[49,91,92] Keeping track of the dorsal pole, the retina was carefully separated from the posterior eyecup. The flattened retina and posterior eyecup were mounted on a SuperFrost Plus microscope slide, using VectaShield Mounting Media with Phalloidin. Using Zeiss LSM 710 Laser Scanning Confocal Microscope with a 10x objective lens, each flat-mounted posterior eye cup was imaged RPE-side facing the lens. The flat mount was imaged by doing a 13 x 13 tile scan with Z-stack acquisition. The pixel dimensions were set to 2048 x 2048 with averaging 2 and scan speed of 8. The flat-mounted retina was simply used as a control for AAV constructs injected with a *CAG* promoter. If the retina did not show green fluorescence, then the RPE sample was not analyzed due to a possibly improper AAV injection.

Within ImageJ, maximum intensity projections were generated for each image. ROI 1-Click Tool was used to manually count each green, fluorescent RPE cell to minimize inaccuracies in quantification due to low GFP-positive (GFP+) RPE counts for some samples. RPE cells were identified as hexagonal shaped cells with a nucleus. Anything that looked green that did not fit this criterion was excluded from counting. Each cohort's cell counts were averaged.

Chapter 3 Novel AAV capsid delivery of therapeutic gene, hRPE65, to RPE65-deficient, rd12 mice

3.1 Introduction

Inherited retinal diseases caused by loss-of-function mutations in the *RPE65* gene represent a compelling target for gene therapy, as restoration of a single, functional enzyme within the RPE is sufficient to reconstitute the visual cycle and halt photoreceptor degeneration. The development of safe and effective delivery strategies for such therapy remains a central challenge in the field. It is important to find a strategy that minimizes surgical risk while maximizing retinal coverage.

Preclinical efficacy for LCA2 gene therapy was established in canine models, where the subretinal delivery of an AAV2 vector packaging a functional *RPE65* gene encoding the retinoid isomerohydrolase RPE65 protein resulted in rapid and sustained restoration of visual function.[18] These findings paved the way for the development of Luxturna, the first FDA approved gene therapy *in vivo* treatment of any disease.[42-48] Clinical results have been beneficial, with treated patients demonstrating improved visual function, most notably an increase in light sensitivity of up to 10,000-fold that is sustained for several years.[93-96] Despite this clinical triumph, the reliance on subretinal injection presents significant limitations to the widespread adoption and safety of retinal gene therapy.

The spontaneously arising *rd12* mouse model for LCA2 has created an avenue for therapeutic testing in this disease. These mice possess an autosomal recessive mutation where cytosine at cDNA position 130 in the *Rpe65* gene is replaced with thymine, resulting in an early stop codon. Like human patients, the RPE65 enzyme is dysfunctional. Without functioning RPE65, the *rd12* mice lack an intact visual cycle, preventing the regeneration of 11-*cis*-retinal for light sensitivity in the photoreceptor outer segments. This leads to rapid cone degeneration beginning at P14 and significantly diminished ERG responses.[11,19,97,98]

Several studies have been previously published, with AAV vectors delivering a normal copy of *RPE65* or *Rpe65* to *rd12* mice for functional rescue. However, these studies were performed using a subretinal injection. To date, functional rescue in *rd12* mice using IVT administration has not been demonstrated. In the last chapter, we identified an AAV2-based capsid, AAV2.Var3, capable of transducing the RPE following IVT delivery. We use AAV2.Var3 to express the therapeutic cDNA, h*RPE65*, in RPE cells. In this way, we can test the therapeutic efficacy of this novel AAV capsid variant in the *rd12* mouse, a model for LCA2.

3.2 Results

3.2.1 AAV2.Var3-CAG-hRPE65 and AAV2.Var3-BEST1-hRPE65 Intravitreal Injection at P14 for rd12 hRPE65 Expression and Visual Cycle Function Rescue

Efficient peripheral RPE transduction of AAV2.Var3 with IVT delivery in both mouse and NHP drove further experiments to package AAV2.Var3 with therapeutic gene, h*RPE65*, for treatment of *rd12* mice. AAV2.Var3 with *CAG* (1.28×10^{14} vg/mL concentration, 2.56×10^{11} vg delivered per eye) and *BEST1* (2.05×10^{14} vg/mL concentration, 4.1×10^{11} vg delivered per eye) was used to deliver non-mutated h*RPE65* at P14 for functional RPE65 expression and visual cycle function preservation in *rd12* mice.

Our control mice included uninjected, AAV2.Var3-*CAG-GFP*, AAV2.Var3-*BEST1-GFP* and PBS -injected mice. For complete restoration of functional RPE65 and 11-*cis*-retinal in photoreceptor outer segments, we waited 8 weeks before expression and visual function analyses. The injection site was at the dorsal region oriented at the top of each image (Figure 3.2.1.1). Immunohistochemistry using anti-RPE65 showed peripheral expression of RPE65 protein in treated eyes with similar transduction patterns as the *GFP* expression experiment. Untreated eyes showed no RPE65 protein expression throughout the flat mount (Figure 3.2.1.1A). Autofluorescence from RPE nuclei is shown, a common histological artifact from a lack of melanosomes in the nuclei compared to the RPE cytoplasm.

Western blot data collected from different cohorts of mice (P14+56) show RPE65 protein present in hRPE65 treated cohorts and the BEST1-GFP treated cohort (Figure 3.2.1.1C). The top band at 65 kDa, or non-truncated RPE65, is quantified and compared relative to *rd12* uninjected mice in the corresponding bar graph. Statistically significant increase in RPE65 expression is seen for the BEST1-hRPE65 treated cohort compared to *rd12* uninjected (***P=0.001), CAG-GFP injected (***P=0.001), BEST1-GFP injected (*P=0.027), and CAG-hRPE65 injected (**P=0.005) mice. The CAG-hRPE65 treated cohort displayed a statistically significant increase in RPE65 protein presence compared to the CAG-GFP injected cohort (*P=0.019). Double bands in the 65 kDa region is likely due to non-specific binding of anti-RPE65. Faint levels of RPE65 protein presence in control groups may be a result of antibody binding to residual, truncated RPE65 in the *rd12* mouse model.

To collect a biochemical readout of restored, functional RPE65 enzymes in *rd12* mice, we conducted high-performance liquid chromatography (HPLC) to quantify *syn*-11-*cis*-retinal oxime and all-*trans*-retinyl ester in untreated and treated *rd12* mice 8-12 weeks after treatment. Figure 3.2.1.1B shows a strong correlation between treatment and reduced accumulation of all-*trans*-retinyl ester. Uninjected *rd12* mice (N=4) demonstrated a high all-*trans*-retinyl ester peak and no *syn*-11-*cis*-retinal oxime (a chemically stabilized 11-*cis*-retinal derivative) peak, meaning that there was an overaccumulation of the retinyl ester and no conversion into 11-*cis*-retinal. For *rd12 CAG/BEST1-*

GFP treated cohorts (N=4/N=3), there is a comparably high peak for all-*trans*-retinyl ester and no peak for *syn*-11-*cis*-retinal. This is important to note because the photopic ERG recordings showed an improved A and B wave amplitudes in response to 3 and 10 cds/m^2 light flash (Figure 3.2.1.1), but the HPLC data shows that there is no detectable 11-*cis*-retinal present in these cohorts. For the *CAG/BEST1*-h*RPE65* treated cohorts (N=4/N=4), there was a much lower all-*trans*-retinyl ester peak and trace amounts of 11-*cis*-retinal in some of the treated mice. Figure 3.2.1.1B displays nmol/eye of each molecule, with a statistically significant reduction of all-*trans*-retinyl ester in AAV2.Var3-CAG-h*RPE65* treated mice (**P*=0.029).

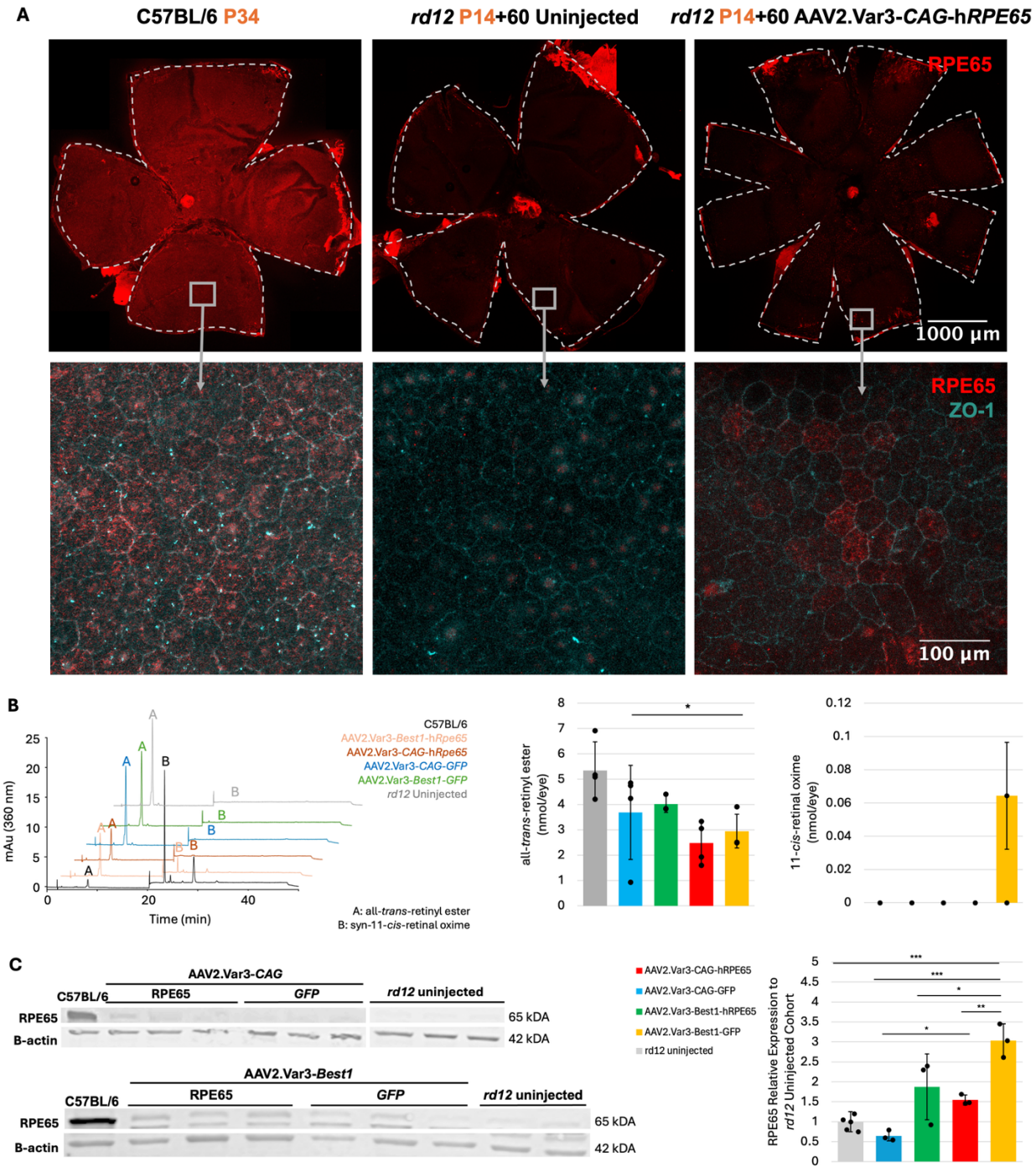

Figure 3.2.1.1 *AAV-induced RPE65 expression and correlating retinoid levels* **(A)** Red shows anti-RPE65 staining for RPE65 protein expression and cyan shows anti-ZO-1 for junctions between RPE. Wildtype C57BL/6 sample shows widespread RPE65 expression as expected. Uninjected rd12 sample 8 weeks after treatment starting time point shows zero RPE65 expression. Autofluorescent regions within the RPE nuclei are seen. Sample treated with AAV2.Var3-CAG-hRPE65 shows patches of RPE65 expression in the periphery. (P14+60 = AAV injection at P14 + enucleation at

P60, noted in Figure 4A). **(B)** Representative, offset HPLC traces show sustained accumulation of all-trans-retinyl ester, labeled A, and no measurable amount of syn-11-cis-retinal oxime, labeled B, in both cohorts entirely for single, control representative samples. For the single representative AAV2.Var3-CAG-hRPE65 trace and AAV2.Var3-BEST1-hRPE65 trace, there was less accumulation of all-trans-retinyl ester and trace amounts of syn-11-cis-retinal oxime. Bar plots of retinyl ester and syn 11-cis-retinal oxime (nmol/eye) for each cohort show a statistically significant reduction in the accumulation of all-trans-retinyl ester for the AAV2.Var3-CAG-hRPE65 treated cohort compared to the AAV2.Var3-CAG-GFP treated cohort, *P=0.029. **(C)** Western blot bands show RPE65 protein present in hRPE65 treated cohorts and the BEST1-GFP treated cohort. Statistically significant increase in RPE65 expression is seen for the BEST1-hRPE65 treated cohort compared to rd12 uninjected (***P=0.001), CAG-GFP injected (***P=0.001), BEST1-GFP injected (*P=0.027), and CAG-hRPE65 injected (**P=0.005) mice. The CAG-hRPE65 treated cohort displayed a statistically significant increase in RPE65 protein presence compared to the CAG-GFP injected cohort (*P=0.019). Statistics conducted using one-way ANOVA with Tukey's HSD post-hoc multiple comparison test. Data shown as mean (SD).

3.2.2 Photopic Visual Function Measured 8 Weeks Post-Injection

To determine whether the increased retinoid expression led to functional recovery of photoreceptors, we performed ERGs with two flash intensities, 3 cds/m^2 and 10 cds/m^2. Being able to visualize A-wave responses from photoreceptors and B-wave responses from inner retinal neurons would display that not only is 11-*cis*-retinal being generated downstream from all-*trans*-retinyl in the visual cycle, but also the light-sensitive chromophore is functional in generating an electrophysiological response. Trace amounts of visual chromophore are regenerated from the AAV-mediated delivery of h*RPE65,* where the amount is below a threshold of detection with the HPLC-based retinoid analyses. Here, the photopic ERG responses were recorded to test if there is an electrophysiological improvement that is quantifiable.

In C57BL/6 mice from this study, B-wave amplitudes in photopic conditions ranged from 60-90 μV in response to 3 cds/m^2 and 60-150 μV in response to 10 cds/m^2 flashes. The uninjected *rd12* mice in our study displayed B-wave amplitudes between a range of 7-12 μV in response to 3 cds/m^2 and 17-28 μV in response to 10 cds/m^2 flashes. Eight weeks after treatment, photopic ERG displayed an increase in B-wave amplitudes for all treated cohorts including *CAG/BEST1-GFP* and *CAG/BEST1*-h*RPE65*, between 12-26 μV in response to 3 cds/m^2 and 17-48 μV in response to 10 cds/m^2 flashes. The AAV2.Var3-*BEST1*-h*RPE65* treated cohort (N=8, Figure 3.2.2.1) displayed the largest increase in B-wave amplitudes in response to both light intensities compared to all other injected cohorts, with no statistical significance. Increased B-wave amplitudes in *GFP*-treated *rd12* mice were observed despite no therapeutic gene expression and no functional RPE65 present.

Alternatively, the PBS-injected cohort displayed reduced B-wave amplitudes in comparison to *rd12* uninjected mice, indicating a rescue phenotype is observed in all AAV2.Var3 injected cohorts only. A-wave amplitudes were not recorded clearly and could not be quantified due to high levels of background noise, reducing the consistency of a baseline amplitude for all measurements.

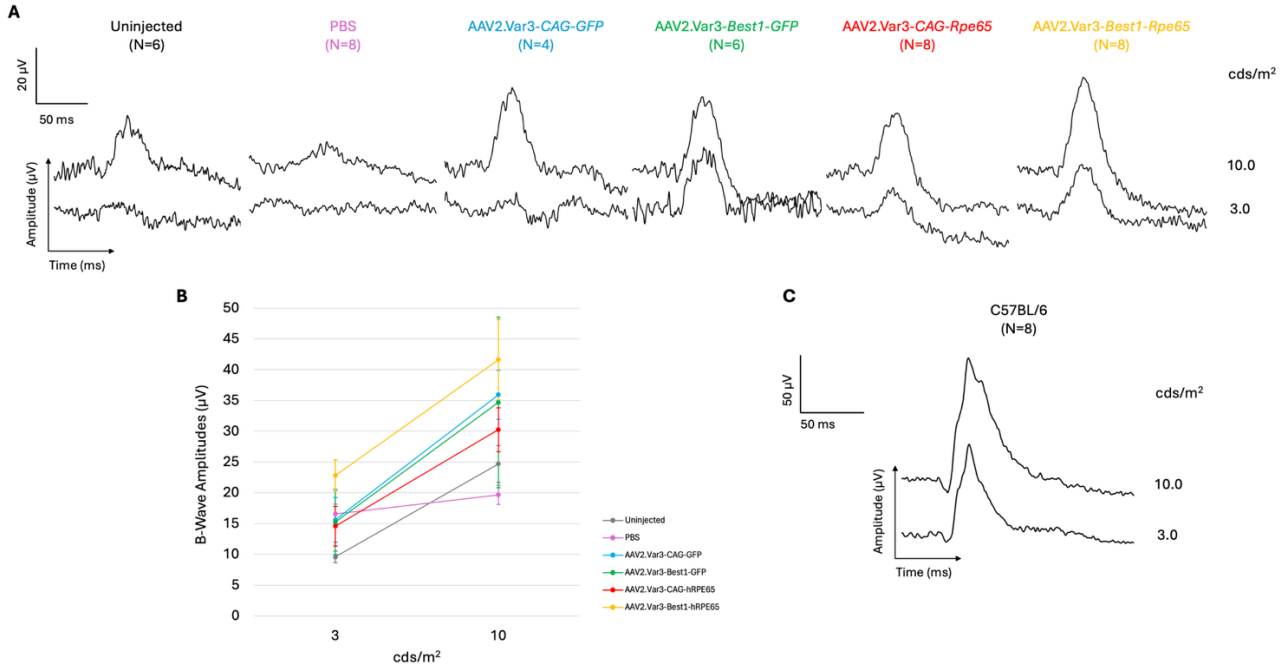

Figure 3.2.2.1 *Photopic ERG amplitudes 8 weeks after P14 treatment of rd12 model with PBS, AAV2.Var3-CAG-hRPE65, AAV2.Var3-BEST1-hRPE65, AAV2.Var3-CAG-GFP, and AAV2.Var3-BEST1-GFP* **(A)** Photopic ERG waveforms averaged for rd12 mice injected with PBS, CAG-Rpe65, BEST1-Rpe65, CAG.GFP, and BEST1.GFP compared with the uninjected rd12 control mice. The bottom trace corresponds to the voltage responses to a 3.0 cds/m^2 light flash. The top trace corresponds to the voltage responses to a 10 cds/m^2 light flash. The light flash occurs at the 0 milliseconds (ms) timepoint and persists for 4 ms. Scale bars provided for amplitude in µV on the y-axis and time in ms on the x-axis. **(B)** Average B-wave amplitudes of each cohort is plotted for comparison. No significance is present for the increase in B-wave amplitudes following AAV treatment compared to the uninjected rd12 cohort. The largest increase is seen in the AAV2.Var3-BEST1-hRPE65 treated cohort compared to the uninjected rd12 mice after a 3 cds/m^2 light flash, P=0.0541, with two-way ANOVA with repeated measures for flash intensity with Tukey's HSD post-hoc test (no significance). Data shown as mean (SEM). **(C)** Wildtype C57BL/6 photopic ERG waveforms averaged for the same light flash intensities. Scale bars provided for amplitude in µV and time in milliseconds.

Figure 3.2.2.2 provides selected individual HPLC traces for each cohort collected for retinoid quantification. Distinct blue arrows in the figure indicate all-*trans*-retinyl ester and *syn*-11-*cis*-retinal oxime peaks within the traces. Most notably, there is a small visible peak present for *syn*-11-*cis*-retinal oxime within all h*RPE65* treated samples, but no visible peak for all control samples. These peaks were below the quantifiable threshold in nanomoles except one of the AAV2.Var3-*BEST1*-h*RPE65* treated mice (R43) which showed the highest detectable level of *syn*-11-*cis*-retinal oxime, shown in the bar graph (Figure 3.2.1.1B) Corresponding ERG recording under photopic conditions are shown for each of the representative HPLC traces. These ERG recordings are from singular eyes treated with the indicated vector. From Figure 3.2.2.1, the uninjected *rd12* mice displayed B-wave amplitudes between a range of 7-12 μV in response to 3 cds/m^2 and 17-28 μV in response to 10 cds/m^2 flashes. Visible *syn* 11-*cis*-retinal oxime peaks at around 23 minutes are seen in slightly improved B-wave amplitudes for the h*RPE65* treated eyes, 50 μV for *CAG*-h*RPE65* and 65 μV for *BEST1*-h*RPE65*. However, despite a lack of a visible *syn* 11-*cis*-retinal oxime peak for the *CAG-GFP* treated eye, there is a notable 41 μV B-wave amplitude following a 10 cds/m^2 flash. The *BEST1-GFP* treated eye show undetectable B-wave amplitudes for both light flash intensities, consistent with the lack of a *syn* 11-*cis*-retinal oxime peak. On average, the photopic ERG results showed maintained or improved B-wave amplitudes, even for both *GFP* treated cohorts. However, PBS treated mice had attenuated B-waves. Figure 3.2.2.2 is an example of variability between injections, where the representative *BEST1-GFP* treated eye is not consistent with the trend seen in the rest of the cohort. However, the *CAG-GFP* treated eye shows this B-wave amplitude improvement. Either the occurrence of an ocular surface penetration during the injection or the presence of a viral capsid within the retinal layers may be producing the minor rescue phenotype.

A

	all-*trans*-retinyl ester (pmol/eye)	11-*cis*-retinal oxime (pmol/eye)
Uninjected	5083.485747	0
	4209.717383	0
	6908.960923	0
	5164.988975	0
AAV2.Var3-*CAG-GFP*	929.9709082	0
	4847.789585	0
	4238.556772	0
	4745.284443	0
AAV2.Var3-*Best1-GFP*	3823.070181	0
	3842.041348	0
	4406.373052	0
AAV2.Var3-*CAG-Rpe65*	1933.565632	0
	1603.01244	0
	3331.184172	0
	3056.892952	0
AAV2.Var3-*Best1-Rpe65*	2486.144817	0
	2507.414209	64.34812927
	3910.839478	0
	2889.768726	0
C57Bl6 Wildtype	247.0915735	436.9521301
	211.8333359	467.4512476
	472.9741058	471.1351782
	295.0640891	464.7889246

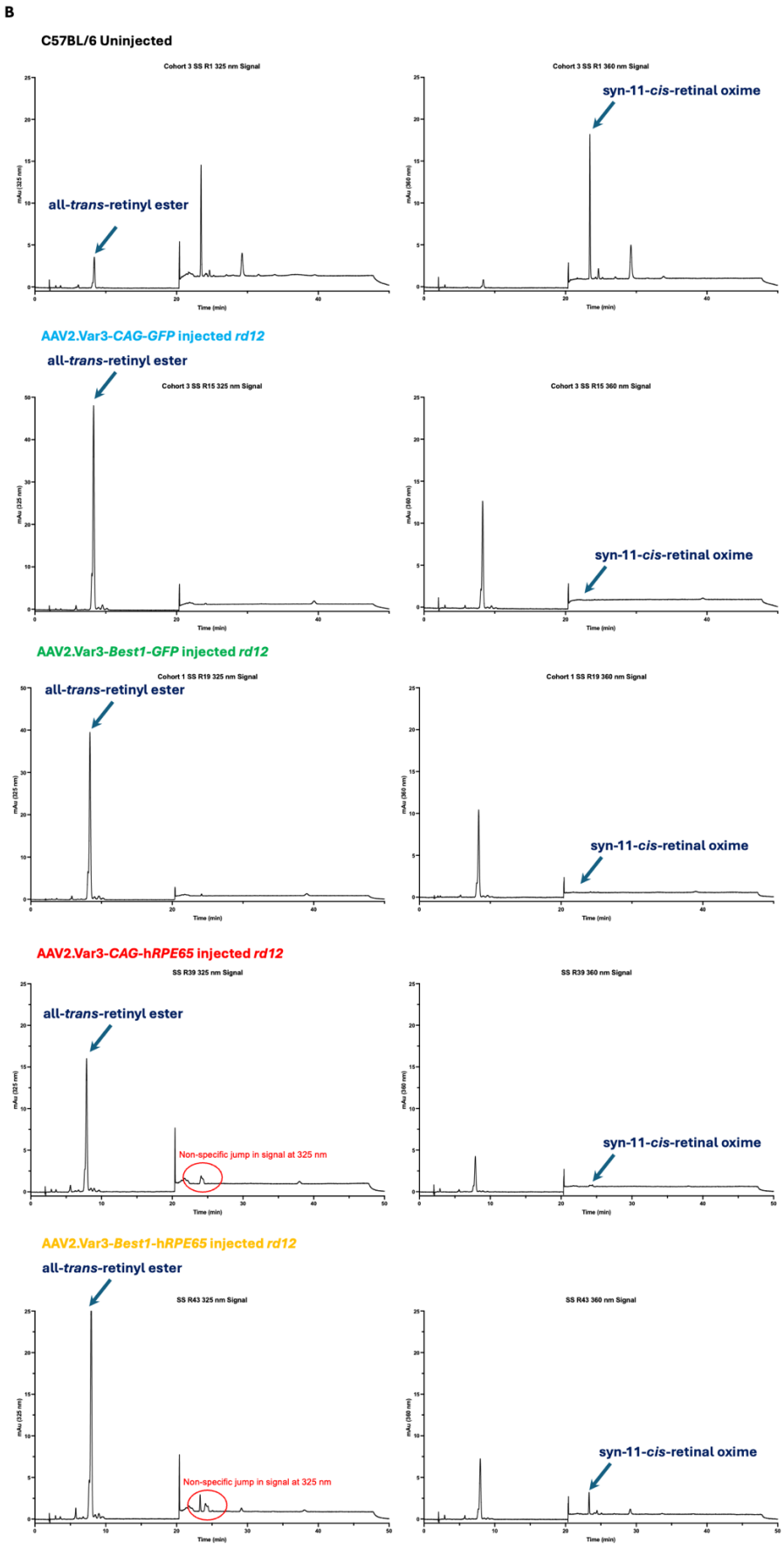
B
C57BL/6 Uninjected
Cohort 3 SS R1 325 nm Signal
Cohort 3 SS R1 360 nm Signal
all-trans-retinyl ester
syn-11-cis-retinal oxime
AAV2.Var3-CAG-GFP injected rd12
all-trans-retinyl ester
Cohort 3 SS R15 325 nm Signal
Cohort 3 SS R15 360 nm Signal
syn-11-cis-retinal oxime
AAV2.Var3-Best1-GFP injected rd12
Cohort 1 SS R19 325 nm Signal
Cohort 1 SS R19 360 nm Signal
all-trans-retinyl ester
syn-11-cis-retinal oxime
AAV2.Var3-CAG-hRPE65 injected rd12
SS R39 325 nm Signal
SS R39 360 nm Signal
all-trans-retinyl ester
Non-specific jump in signal at 325 nm
syn-11-cis-retinal oxime
AAV2.Var3-Best1-hRPE65 injected rd12
all-trans-retinyl ester
SS R43 325 nm Signal
SS R43 360 nm Signal
Non-specific jump in signal at 325 nm
syn-11-cis-retinal oxime
Time (min)

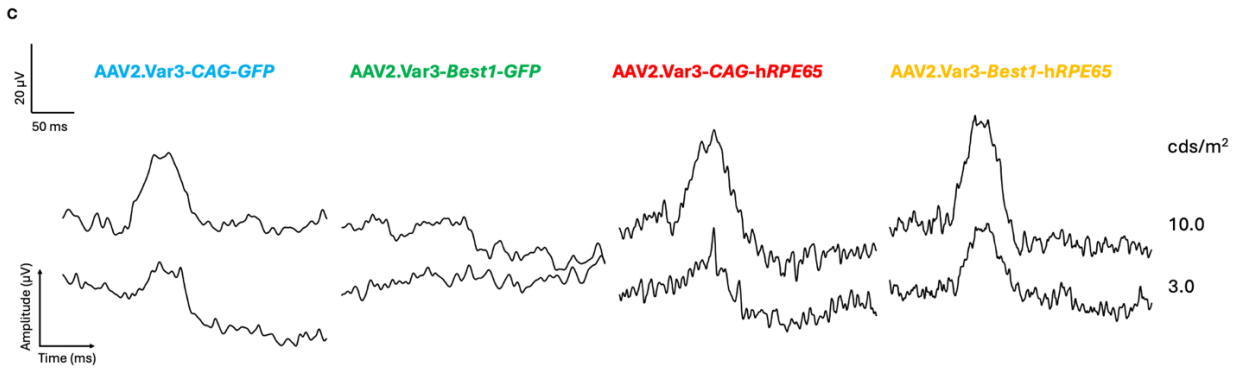

Figure 3.2.2.2 *HPLC retinoid quantification with corresponding photopic ERG recordings* **(A)** *Rd12* mice eyes were analyzed for retinoid quantification of all-*trans*-retinyl ester and 11-*cis*-retinal oxime (pmol/eye) for each cohort. **(B)** Most h*RPE65* treated cohorts had samples with trace levels of 11-*cis*-retinal oxime represented by peaks, but these were below threshold and thus not quantifiable. R1: *C57BL/6* wildtype, R15: *rd12* AAV2.Var3-*CAG-GFP* treated, R19: AAV2.Var3-*BEST1-GFP* treated, R39: AAV2.Var3-*CAG-hRPE65* treated, R43: AAV2.Var3-*BEST1-hRPE65* treated. **(C)** Single mouse eye ERG recordings from corresponding HPLC samples in **B**.

3.2.3 Scotopic Visual Function Measured 8 Weeks Post-Injection

Rod function may have interference with the photopic ERG waves recorded, since *rd12* mice have slower degeneration of rods than cones.[97] Additionally, just 2% of mouse photoreceptors are cones making rod-derived signal in photopic ERG inevitable.[99] To partially mitigate this possibility, scotopic ERG, measuring rod-mediated responses under dark-adapted conditions, was performed in parallel, allowing rod and cone contributions to retinal function to be assessed independently and providing a more complete picture of photoreceptor rescue across both cell types. We measured response to dim light flash levels of 0.01, 0.1, and 1 cds/m^2 after overnight dark adaption. AAV2.Var3-*CAG*-h*RPE65* and AAV2.Var3-*BEST1*-h*RPE65* both displayed increased A-wave and B-wave amplitudes on average 8 weeks after IVT injection, compared to the *rd12* uninjected, PBS and GFP treated cohorts. The AAV2.Var3-*CAG-GFP* treated group exhibited an increase in A-wave amplitudes in Figure 3.2.3.1B, however, like the photopic ERG recording, there is reduced consistency of a baseline recording for this group and all other control groups. The h*RPE65* treated cohorts displayed the largest reduction in background noise and most reliable baseline recording. The explanation for reduced background noise in h*RPR65* treated cohorts in unclear.

C57BL/6 mice from this study had A-wave amplitudes between 43-75 µV (0.01 cds/m^2), 99-104 µV (0.1 cds/m^2), and 183-376 µV (1 cds/m^2). The wildtype C57BL/6 B-wave amplitudes occurred between 247-468 µV (0.01 cds/m^2), 501-532 µV (0.1 cds/m^2), and 487-670 µV (1 cds/m^2). The uninjected *rd12* mice had no quantifiable A-wave amplitudes. However, the uninjected *rd12* B-

wave amplitudes ranged between 18-30 μV (0.01 cds/m^2), 13-19 μV (0.1 cds/m^2), and 24-49 μV (1 cds/m^2). Notably, from the B-wave amplitudes, statistical significance was seen for the AAV2.Var3-*CAG*-h*RPE65* treated cohort compared to uninjected (***P<0.0001), PBS treated (*P=0.0425), and AAV2.Var3-*BEST1-GFP* treated (***P=0.0007) *rd12* mice where the response ranged from 23-70 μV and the AAV2.Var3-*BEST1*-h*RPE65* treated cohort compared to uninjected *rd12* mice (*P=0.0145) where the response ranged from 25-37 μV after a 0.1 cds/m^2 flash. The difference in mean between the AAV2.Var3-*CAG*-h*RPE65* treated cohort and the *rd12* uninjected cohort was approximately 42 μV for the 0.01 cds/m^2 flash, 35 μV for the 0.1 cds/m^2 flash, and 50 μV for the 1.0 cds/m^2 flash.

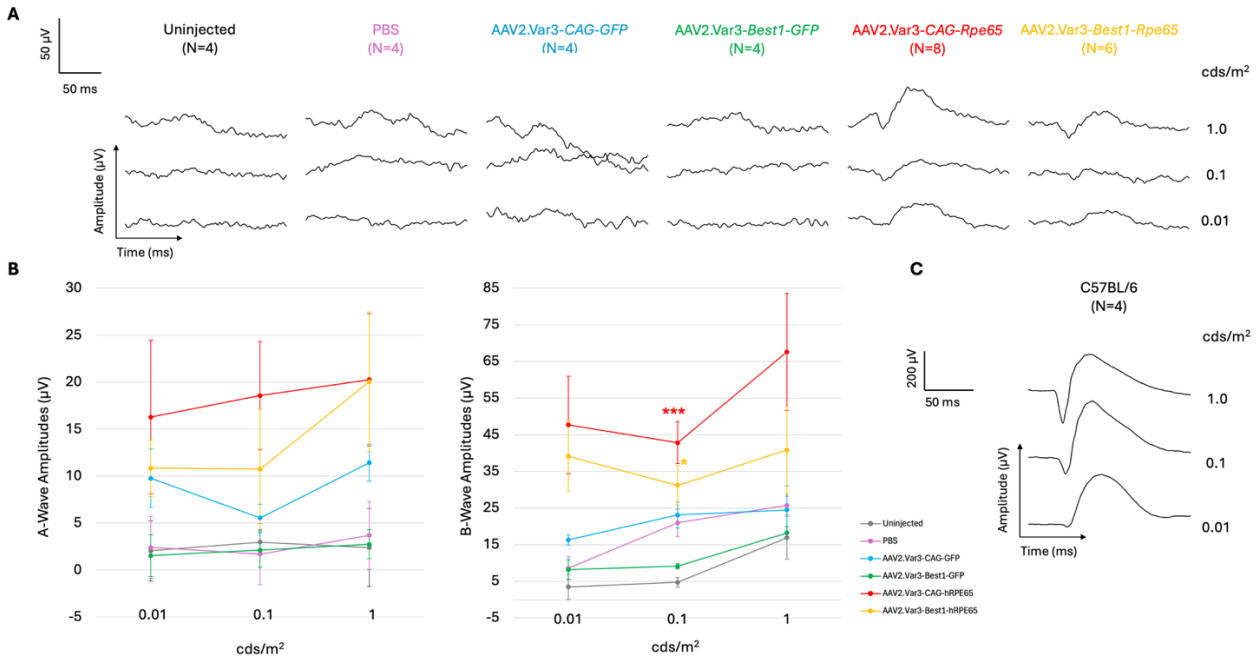

Figure 3.2.3.1 *Improved scotopic ERG amplitudes 8 weeks after P14 treatment of rd12 model with AAV2.Var3-CAG-hRPE65 and AAV2.Var3-BEST1-hRPE65* **(A)** Scotopic ERG waves plotted for comparison between uninjected and PBS, CAG-GFP, BEST1-GFP, CAG-hRPE65, BEST1-hRPE65 treated rd12 mice when tested at 0.01, 0.1, and 1.0 cds/m^2 light flashes. The light flash occurs at the 0 milliseconds (ms) timepoint and persists for 4 ms. **(B)** A-wave amplitudes increased on average for the CAG-hRPE65 treated cohort at all flash intensities compared to the uninjected rd12 and CAG-GFP /BEST1-GFP-injected cohorts. No significant pairwise differences identified. B-wave amplitudes increased on average for both hRPE65-treated cohorts at all flash intensities. Statistical significance was seen for the AAV2.Var3-CAG-hRPE65 treated cohort compared to uninjected (***P<0.0001), PBS treated (*P=0.0425), and AAV2.Var3-BEST1-GFP treated (***P=0.0007) rd12 mice and the AAV2.Var3-BEST1-hRPE65 treated cohort compared to uninjected rd12 mice (*P=0.0145). Statistics conducted with two-way ANOVA with repeated measures for flash intensity with Tukey's HSD post-hoc test. Data shown as mean (SEM). **(C)** Wildtype C57BL/6 scotopic ERG waveforms averaged for the same light flash intensities. Scale bars

provided for amplitude in μV and time in milliseconds.

3.2.4 Measuring Cone Survival After Restored h*RPE65* Expression

To determine if the observed functional recovery correlated with structural preservation, we quantified medium wavelength (MW) -opsins and short wavelength (SW) -opsins as a measure for cone survival. In *rd12* mice, cone degeneration begins at P14 and progresses past P90. Cone degeneration is not equally spread across the retina, but rather occurs predominantly in the nasal and ventral quadrants of the retina while dorsal and temporal quadrant cones are highly preserved.[100] In addition, MW-opsin cones are equally distributed across the mouse retina, while SW-opsin is found mostly nasal and ventral, from histology performed in C57BL/6 retina shown in Figure 3.2.4.1A.

Due to the high number of overall cones in the mouse retina, we quantified using 13 subareas in the retina, 3 in each quadrant and 1 at the optic nerve. Each of the subareas was a 304.5 μm x 304.5 μm square which is roughly 5% of the surface area of an entire mouse retina. With 13 sub-square images, we quantified about 65% of the total retina to get representative quantification of the cone distribution. For each of the 3 collected images in each quadrant we took an image at the periphery, midperiphery, and central retina. Our results indicated that the overall highest increase in cone survival was observed at the midperiphery of the dorsal quadrant which is nearest to the injection site. However, no other correlation with eccentricity and cone survival was seen following AAV2.Var3-*CAG*-h*RPE65* and AAV2.Var3-*BEST1*-h*RPE65* treatment. There was a slight increase in SW-opsin cone survival for our AAV2.Var3-*BEST1*-h*RPE65* treated cohort, with a lot of variability between retinas. Despite a statistically significant increase in RPE65 expression in AAV2.Var3-*BEST1*-h*RPE65* treated mice, no correlation was found between enzyme restoration and cone survival. High levels of opsin mis localization to the inner segments in all cohorts was observed.

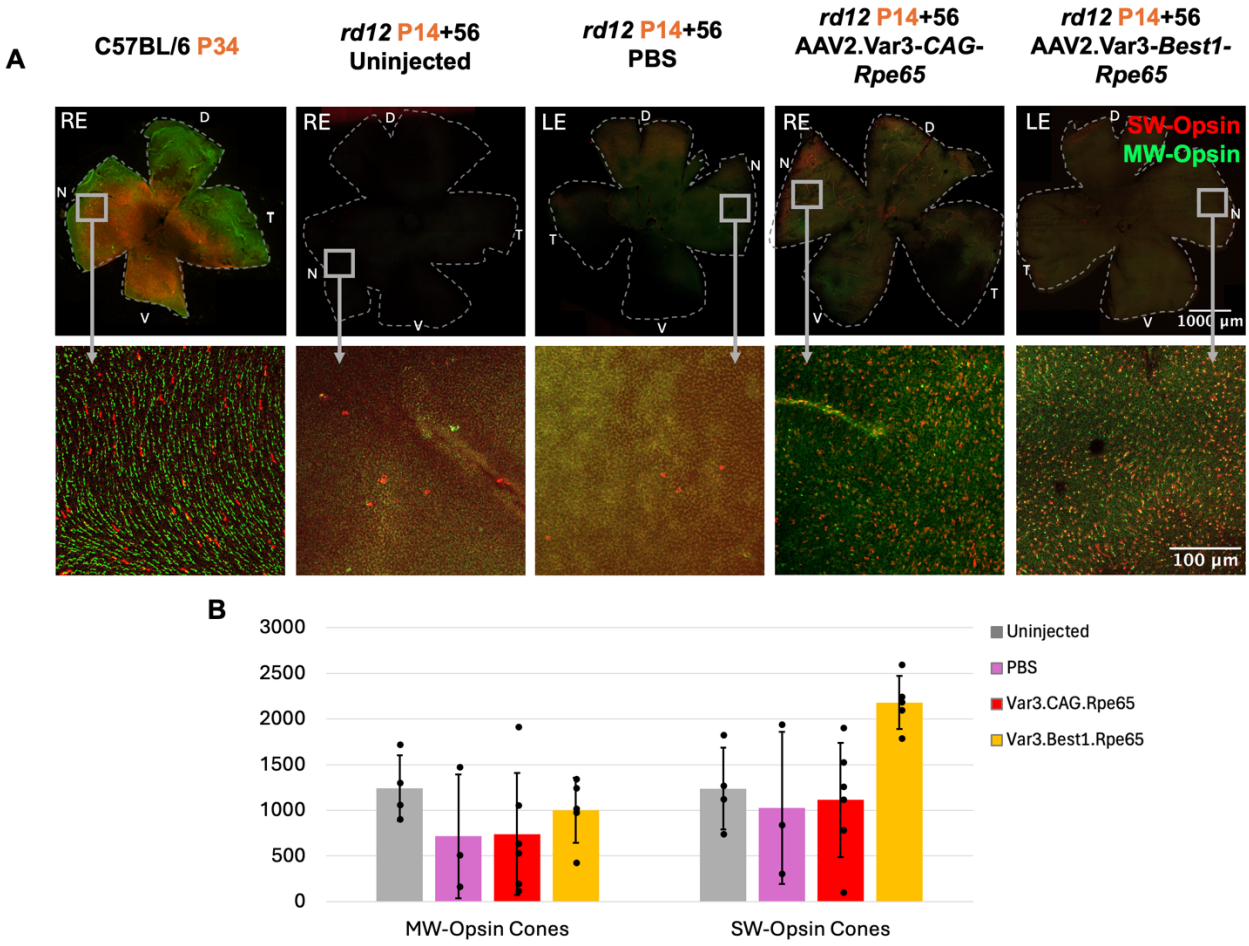

Figure 3.2.4.1 *Cone quantification 8 weeks after P14 treatment of rd12 model with PBS, AAV2.Var3-CAG-hRPE65 and AAV2.Var3-BEST1-Rpe65* **(A)** Flat mounted retinas from C57BL/6 mouse, rd12 uninjected (N=4), PBS (N=3), CAG- (N=6), and BEST1- (N=5) hRPE65 treated cohorts display cone landscape 8 weeks post-treatment. Nasal quadrant images (319.45 x 319.45 µm) display comparison of SW-opsin and MW-opsin distribution between control and treatment groups. **(B)** Cone quantification data based on SW-opsin and MW-opsin antibody probed cones is averaged. The y-axis displays the number of individual cones quantified with a fluorescent marker. Quantification data shows similar distribution of opsins across all groups with no statistical significance in cone survival. Data shown as mean (SD).

3.2.5 Assessing Light-Responsive Behavior of Mice After Restored RPE65 Expression

After slight improvements in visual function displayed by ERG results, it was important to assess whether the small improvements in voltage response of photoreceptors and inner retinal neurons are correlated with behavioral changes in response to light. In other words, behavior assays

can show whether cellular-level changes are enough to enhance the visual experience of the animal being treated, especially when the treatment model is not a human that can verbalize their visual experience. A two-chamber box is used in this assay where the two chambers are separated by a wall with a small opening for a mouse to crawl through. The assay helps determine if the mouse can see light at a specific luminance level based on if the mouse is avoiding the chamber that is lit. A habituation stage is performed before the experimental run to determine which chamber the mouse naturally prefers to be on. It is important to note that mice biologically prefer to be in dim or dark environments where they are not exposed to potential predators.

In Figure 3.2.5.1, there was no evidence that the minor improvements in visual function from the ERG correlated with behavioral changes in light avoidance. The luminance level of the light delivered to the two-chamber box was equivalent to that of the average bright office light. Despite some restored expression of the RPE65 enzyme within peripheral photoreceptors, a statistically significant increase in RPE65 protein expression, and a demonstrated reduced accumulation of all-*trans*-retinyl ester, these changes were not enough to affect the visual experience of the mice treated. The luminance levels for the ERG assays ranged from 0.01-10 cds/m^2 which, while not directly interchangeable, roughly equate to a range of 0.001-1000 lux. For the light avoidance assay, using a 900-lux luminance level elicits a photopic response, while most of the improved visual function with h*RPE65* treatment was seen with scotopic vision. A limitation within this assay was not testing a range of luminance levels below 900-lux for analysis of behavior response changes. It is also important to note that uninjected *rd12* mice have a level of light perception that remains despite degeneration progressing. This is evident from the B-wave amplitude in response to 10 cds/m^2 light in Figure 3.2.2.1 where this luminance is roughly in the same range as that delivered for the light avoidance assay.

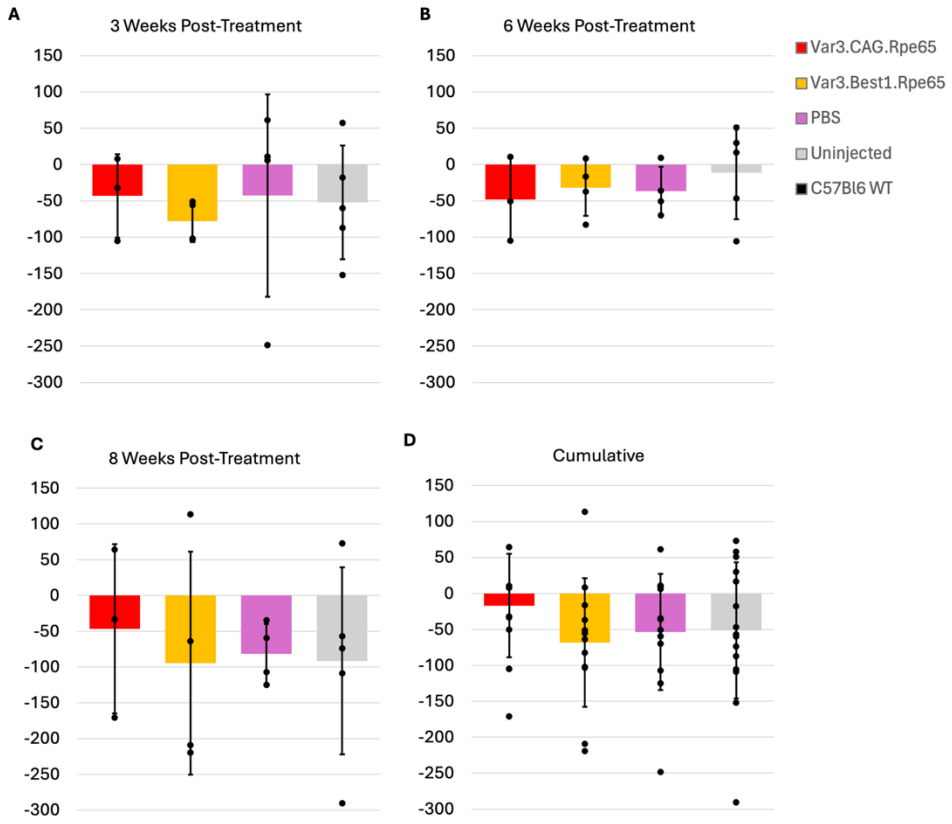

Figure 3.2.5.1 *Light avoidance of rd12 mice in a two-chamber box at 3-, 6-, and 8-weeks post-treatment with AAV2.Var3-CAG-*h*RPE65, AAV2.Var3-BEST1-*h*RPE65, and PBS* **(A)** 3 weeks post-treatment AAV2.Var3-BEST1-h*RPE65* (N=4) had the highest change in preferred side with the lowest variation between samples. *Rd12* uninjected (N=5), PBS (N=4), and AAV2.Var3-*CAG*-h*RPE65* injected (N=3) had reduced change in preferred side in. **(B)** 6 weeks post-treatment change in preferred side reduced overall with no statistical significance between cohorts. **(C)** 8 weeks post-treatment no significant light avoidance behavior was observed. **(D)** Combined data from 3-, 6-, and 8-weeks post-treatment shows no statistical significance in change in time spent on preferred side of the box. Data shown as mean (SD).

3.3 Discussion

Therapeutic capabilities of the novel capsid, AAV2.Var3, are outlined in this series of functional and expression-based assays. In general, transgene expression levels are not always replicated between capsids used, transgenes packaged, and cell type targeted. With multiple variables at play, like intracellular trafficking and protein translation, expression can vary. Experiments shown in this chapter give confidence that transgene expression is similar when both AAV2.Var3-

CAG/BEST1-GFP and AAV2.Var3-CAG/*BEST1*-h*RPE65* are delivered. Approximately 10% of RPE cells expressing functional RPE65, based on quantification results from GFP expression quantification (Figure 2.2.2.2). Subsequently, 11-*cis*-retinal production in *rd12* mice was determined to be around 15% of that in C57BL/6 wildtype mice and all-*trans*-retinyl ester accumulation was reduced by almost half compared to that of *rd12* uninjected mice. Concomitant minor improvements in the ERG results is consistent with prior LCA2 gene therapy studies where modest biochemical rescue was sufficient to produce meaningful improvements in visual function.[17,52]

Restored light-sensitive chromophore leads to improved photopic and scotopic ERG responses to dim light flashes between 0.01 cds/m^2 and 10 cds/m^2. Notably, there are improvements in scotopic ERG responses within the h*RPE65*-treated cohorts. At 0.1 cds/m^2 light flash, there was a statistically significant improvement in the B-wave amplitude for the AAV2.Var3-*CAG*-h*RPE65* treated cohort (**P*=0.0103). Alternatively, AAV2.Var3-*BEST1*-h*RPE65* showed increased SW-opsin cone survival. These findings mimic clinical observations of RPE65-LCA patients experiencing functional improvements and increased light sensitivity while underlying retinal degeneration continues.[53]

Despite the greater success of RPE transduction with AAV2.Var3-*CAG-GFP*, our therapeutic gene delivery assays display consistently improved protein expression, visual function, and cone survival with AAV2.Var3-*BEST1*-h*RPE65*. This underscores the importance of combining capsid engineering with cell-specific promoters to optimize efficacy. Prior studies have shown that using cell-specific promoters in a therapeutic context can minimize off-target effects and enhance therapeutic gene expression.[101]

These results shed light on the limitations present with anatomical barriers in RPE transduction with IVT injection. Although 10% RPE transduction efficiency is a drastic step forward in the field of IVT delivery, there is still much to be investigated regarding increasing efficiency. Current studies continue to explore dual-therapy options; however, few have overcome the ability to bypass all retinal neurons with one singular capsid, making AAV2.Var3 novel.[11,31] Additionally, transduction efficiency is not near the level achieved with a subretinal injection, making the more invasive subretinal administration method the preferred route for the most efficient therapy. It is worth acknowledging, however, that IVT delivery is associated with greater inflammatory response compared to subretinal injection. Vectors delivered to the subretinal space are more shielded from systemic immune protection, while IVT injection can trigger innate immune responses and can increase the risk of infiltration of neutralizing antibodies.[102,103] Immunosuppressive regimens are usually necessary to mitigate these effects.[104] However, a shift towards delivery that does not damage retinal tissue is essential. Unlike the subretinal surgery, IVT injection is an outpatient procedure. Not only would IVT delivery be less invasive, but also it requires far less surgical training making it far more accessible to patients.[49,105] The clinical implications of AAV2.Var3 are significant for all RPE-associated inherited retinal diseases and would advance the field of retinal gene therapy worldwide.

3.4 Materials and Methods

3.4.1 Immunohistochemistry for Cone Quantification and RPE65 Expression

Eyes were enucleated 8 weeks post-treatment and fixed in 10% formalin for 1 hour at 4ºC. Eyes were washed with PBS 3 times and stored at 4ºC until the immunohistochemistry protocol was performed. Eyes were dissected to separate the retina and posterior eyecup; both were flattened with 4 evenly spaced cuts. Using a 24-well plate, the tissue was washed 3 times with 1 mL PBS + 0.5% TritonX-100. The blocking buffer was 1 mL 5% Normal Donkey Serum incubated with the tissue for 1 hour at 4ºC.

For cone quantification, primary antibody staining was performed using 1:500 Anti-Opsin Red/Green rabbit polyclonal (Merck Millipore AB5405, Lot: 4218891) and 1:500 Anti-Opn1SW goat polyclonal (Santa Cruz Biotechnology SC-14363, Lot: L0811) overnight, followed by 3 washes with 1 mL PBS + 0.5% TritonX-100. Secondary antibody staining was performed for 1 hour using 1:500 Donkey Anti-Rabbit Alexa Fluor 594 (Invitrogen A-21207, Lot: 2145022) and 1:500 Donkey Anti-Goat IgG (H+L) Alexa Fluor 647 (Invitrogen A-21447, Lot: 2841625). All tissue was washed 3 times with PBS prior to mounting on a microscope slide. Using a 20x objective lens on a laser scanning confocal microscope (Zeiss LSM 990 AxioObserver), 13 images (304.5 μm x 304.5 μm) are acquired equidistant from each other, one image at the optic nerve and 3 images for each "petal" of the retinal flat mount. Z-stack acquisition was done within the photoreceptor outer segment layer. Using ImageJ Analyze Particles feature, each cone outer segment was quantified.

For RPE65 expression visualization, primary antibody staining was performed using 1:500 Anti-RPE65 rabbit polyclonal (Invitrogen PA5-78414, Lot: ZK4558857) and 1:500 Anti-ZO-1 mouse monoclonal (Invitrogen 33-9100, Lot: AD410752) overnight, followed by 3 washes with 1 mL PBS + 0.5% TritonX-100. Secondary antibody staining was performed for 1 hour using 1:500 Donkey Anti-Rabbit Alexa Fluor 488 (Invitrogen A-21206, Lot: 2072687) and 1:500 Donkey Anti-Mouse Alexa Fluor 594 (Invitrogen A-21203, Lot: 2069656). All tissue was washed 3 times with PBS prior to mounting on a microscope slide. Using a 10x objective lens on the same laser scanning confocal microscope, a 13 x 13 tile scan was done for the entire flat-mounted posterior eyecup. Z-stack acquisition was done to account for uneven surfaces due to mounting within the RPE layer.

3.4.2 11-*cis*-retinal Quantification

We conducted HPLC to quantify *syn*-11-*cis*-retinal oxime and all-*trans*-retinyl ester in untreated and treated *rd12* mice 8-12 weeks after treatment. Left eyes of all cohorts were processed

for retinoid analyses, while right eyes were kept for cone quantification and RPE65 immunohistochemical expression analysis. Mice were dark adapted for 2 days prior to enucleation to stabilize 11-*cis*-retinal levels. C57BL/6 mice were used as a positive control for standard levels of each molecule. All retinoid analyses were performed under dim red light using the methods in Golczak *et al.*, 2010 and Engfer *et al.* 2025.[106,107] The 11-*cis*-retinal in crude eye homogenates was chemically stabilized as 11-*cis*-retinal oxime via treatment with hydroxylamine prior to retinoid extraction and analysis on an Infinity II series LC instrument (Agilent, Santa Clara, CA) with an attached Agilent Rx-SIL column (cat #: 880975-901, Neta Scientific, Hainesport, NJ). Retinoid peaks that were below the threshold for automatic peak integration were counted as undetectable (0). Areas under the peaks were multiplied by conversion factors derived from standard curves for all-*trans*-retinyl esters and *syn*-11-*cis*-retinal oxime, all dissolved in hexanes, to quantify each retinoid in units of pmol/eye.

3.4.3 Western Blot for RPE65 Protein Quantification

Two mouse eyecups from each mouse were pooled and placed in 1X cell lysis buffer (Cell Signaling Technology #98035) with 1:100 protease & phosphatase inhibitor cocktail. After brief sonication until complete homogenization, the samples were centrifuged at 16,000 rcf for 20 minutes at 4ºC. Supernatants were collected for protein quantification using the Pierce BCA Protein Assay Kit (Thermo Fisher, 23225). For each sample, 20 μg of protein are combined with loading dye (4X Laemmli [BioRad #1610747] + 1:20 2-mercaptoethanol) and water for a total volume of 20 μL. After boiling the samples at 100ºC for 5 minutes, they are loaded into a 10% Mini Protean TGX Gel (BioRad, #4561034) and ran for 1 hour. Gels are transferred to a PVDF membrane (BioRad, #1620174) for 1 hour. The membrane was blocked for 1 hour using TBS blocking buffer (Licor, #NC1660550). Primary antibodies, anti-RPE65 (Invitrogen, #PA5-78414; Lot: 79745935) and anti-beta-Actin (Cell Signaling Technology, #3700TS; Lot: 23), were incubated overnight at 4ºC at a 1:1000 concentration to equal parts 1X TBS and Licor Intercept TBS blocking buffer. Secondary antibodies, IRDye® 800CW Goat anti-Mouse IgG (Licor, #926-32210) and IRDye® 680RD Goat anti-Rabbit IgG (Licor, #926-68071), were incubated for 1 hour at room temperature at a 1:10000 concentration to equal parts 1X TBS and Licor Intercept TBS blocking buffer. Three washes for 5 minutes each with TBS-T were performed after each antibody incubation period. Membranes were imaged using a Licor Infrared Odyssey Imaging System. Acquired images were converted to 8-bit greyscale and inverted. RPE65 and beta-Actin bands were quantified at 65 kDa and 42 kDa, respectively. A histogram was generated for each lane inclusive of all samples within one molecular weight area. The peaks of the histogram are determined by contrast intensity within ImageJ, using the Gels > Plot lanes tool. The area under each peak was measured and normalized to the control to quantify relative RPE65 protein expression compared to *rd12* uninjected controls.

3.4.4 Electroretinogram and Ophthalmic Imaging Protocol

Mice were anesthetized using 100 mg/kg ketamine hydrochloride and 10 mg/kg xylazine. Approximately 50 μL drops of proparacaine, tropicamide, and phenylephrine were added separately to the surface of both eyes, letting each sit for 3 minutes. Drops were removed after 3 minutes with surgical spears. GenTeal(R) Tears Lubricant Eye Ointment was minimally applied to the surface of the eye. Using surgical spears doused in 70% ethanol, the electrode surfaces were wiped clean of any debris. The anesthetized mouse was placed onto the heated Celeris surface, keeping the head and front legs on the raised pedestal. The hind legs and tail were positioned as straight as possible, preventing the back from being hunched. After placing a minimal amount of GenTeal Tears on the electrode surface, the electrodes were placed onto the corneas of the mouse, leaving approximately 1 mm of space and not applying any pressure to the eye. Impedance values were recorded (4-10K). We ran the "Phototopic ERG + OPs" (OP = oscillatory potential) protocol using the default settings from Diagnosys. This protocol collected responses to a 3 cds/m^2 flash and a 10 cds/m^2 flash. Results give strong cone responses without over saturation. This also surpasses the level of over saturation for rod photoreceptors. For scotopic ERG data collection, we ran the "Dark Adapted ERG + OPs" protocol using the default settings from Diagnosys. Results displayed include standard full field responses to 0.01 cds/m^2, 0.1 cds/m^2 and 1.0 cds/m^2 flashes, giving rod responses without cone activation. Flicker and OP responses were not used in the ERG results and analysis. Data was graphed using Igor.

For rhesus macaque, while the animal was sedated, the eyes were dilated using tropicamide ophthalmic solution (Somerset Therapeutics, Hollywood, FL, USA) and phenylephrine hydrochloride ophthalmic solution (Paragon BioTeck, Portland, OR, USA) in preparation for electroretinogram and ophthalmic imaging acquisition. The RETevet device (LKC Technologies, Inc., Gaithersburg, MD, USA) was used. Photopic ERGs responses were captured using a 3 cds/m^2 flash; a 30 hertz (Hz) photopic flicker response was also obtained at that light intensity. Measurements were recorded and presented using the manufacturer's software. Spectral-domain optical coherence tomography (SD- OCT) images were obtained using Heidelberg Explorer software (version 1.8.6.0; Heidelberg Engineering, Heidelberg, Germany). Last, macaques were photographed to obtain color fundus photography images using a Canon CF-1 Retinal Camera with a 50-degree wide-angle lens.

3.4.5 Passive Light Avoidance Assay for Behavioral Analysis

Mice habituated to a two-compartment box (Colbourn Instruments, USA) for 15 minutes in the dark. A floodlight was attached to their preferred compartment. For 15 minutes at a time, mice were recorded and tracked on which compartment they ventured into, initiating the timer once the mouse entered their preferred compartment. A low light intensity of 900 lux was illuminated into the preferred compartment every time the mouse entered. Mice were tracked using sensors at the base

of the box to track the time spent on each side. The experimenter was masked to all cohorts. The change of side preference was quantified based on the change in time a mouse spends on its initially preferred side (determined during the habituation trial) between habituation and the experimental trial. A positive value indicates that the animal spent less time on its previously preferred side during the experimental trial, suggesting light avoidance. A negative value indicates that the animal spent more time on the initially preferred side during the experimental trial, implying that light had no effect on avoidance.

3.4.6 Statistical Analysis

Data is represented as mean ± SD unless otherwise stated. Cohorts were analyzed using one-way ANOVA followed by Tukey's post hoc multiple comparison test to compare treatment groups for GFP+ RPE quantification, western blot, and HPLC data. For electroretinogram data, two-way repeated measures ANOVA were conducted. Each eye was treated as an independent sample, except for western blot where 2 eyes pooled were treated as one sample. Statistical tests were completed using Python scripts (Python version 3.10, run in Spyder IDE within the Anaconda.Navigator distribution; NumPy, Pandas libraries). Statistical significance threshold was set to $P < 0.05$.

Chapter 4 Conclusions

The overall findings of this thesis address one of the largest limitations of ocular gene therapy. For decades, IVT delivery of AAV capsids has not been able to achieve efficient RPE transduction. Through just one round of a high-throughput screening encompassing 1.28 x 10^9 AAV capsid variants in both mouse and non-human primate, this work uncovered a novel capsid that accomplishes this goal. AAV2.Var3 contains a 10 AA peptide insertion (LANQEHVKNA) at AA588 which disrupts the HSPG binding residue of the capsid. This resulted in 10% RPE transduction efficiency proven in both mouse and NHP. With 2.56-4.1 x 10^{11} vg in mouse and 5.8 x 10^{12} in NHP delivered, there is four-quadrant expression of the transgene, as opposed to subretinal delivery where expression tends to remain localized to the bleb region. The current benchmark AAV2-based capsid, AAV2.7m8, efficiently transduces inner retinal neurons and achieves a variable level of photoreceptor transduction with IVT injection. When it comes to RPE transduction, AAV2.7m8 is highly inconsistent and at its best it is not at the level of AAV2.Var3 within this study. The most impactful finding is that the transduction patterns of AAV2.Var3 in mouse are mimicked when delivered to NHP. Although the number of vector genomes delivered in NHP is higher than in mouse, the volumes are high disproportionate. The volume of the average adult mouse vitreous humor is 4-5 μL while for an NHP macaque it can be 2 mL.[108] This makes the macaque's vitreous space 400 times that of the mouse, however, the number of vector genomes delivered is only 12 times higher for the macaque compared to the mouse. Titer plays a large role in AAV therapeutics, where higher titers can result in higher immune reactivity, so achieving optimal transduction with the lowest possible titer is crucial. According to the US Food and Drug Administration, approximately 1.5 x 10^{11} vg are delivered with the subretinal delivery of Luxturna. The dose demonstrated in this study for the NHP IVT delivery is 34 times higher than Luxturna's, however, the subretinal space can retain a volume of around 35 μL on average making the delivery space 57 times smaller than the vitreous space. Accounting for capsid leakage out of the injection hole or through the trabecular meshwork to the anterior chamber, the difference in dose delivery is not proportionate. This demonstrates that the vector genomes delivered with AAV2.Var3-*BEST1-GFP* to the NHP eye are not dramatically increased to optimize efficiency. However, it is important to note that the left eye treated with AAV2.Var3 at a lower dose (1.5 x 10^{12} vg) did not display GFP expression within the RPE layer, making the optimal delivery dosage around 5.8 x 10^{12} vg.

AAV2.Var3 seemingly traversed the retinal neuron to transduce RPE cells, without any dual therapy of enzymes to modify the ILM barrier. The peptide insertion is what is hypothesized to allow for better migration past the ILM with reduced HSPG binding. The outer surface structural modifications of the AAV capsid favors RPE cell entry and transgene expression, equally in mouse and NHP. The strong peripheral transduction pattern shows that there may be anatomical differences at play that make peripheral transduction easier than in the central retina. Presumably the thickness of the ILM is what determines AAV2.Var3 diffusion. However, ILM properties need to be further investigated as there is not much evidence regarding large thickness differences in the central vs. peripheral mouse ILM.

The therapeutic relevance of this capsid was validated with several expression and functional assays in *rd12* mice. Between capsid migration, cell surface tropism, intracellular trafficking, transgene expression, and protein translation, not all AAV capsid perform the same way. It is important to validate the various steps of capsid performance to demonstrate therapeutic capabilities. In this way, we were able to show that AAV2.Var3 can efficiently express h*RPE65* in peripheral RPE cells the same way *GFP* expression was illustrated. Following this, there was proven RPE65 expression in treated mice was shown on western blots. Lastly, the functional assessments using photopic and scotopic ERG show that slight changes in photoreceptor and inner retinal neuron performance can be seen with the treatment of h*RPE65*. While transduction efficiency remains below what subretinal injection can achieve, our capsid displays a level of therapeutic rescue with IVT delivery that has not been shown before.

The clinical implications of AAV2.Var3 extend beyond LCA2 patients, but rather various inherited retinal diseases that affect the RPE, like dry AMD, choroideremia, and bestrophinopathies. Each of these diseases is correlated with mutations in RPE-specific gene expression. These are highly prevalent diseases, affecting millions of people worldwide. Patients with these diseases would benefit greatly from AAV-mediated gene therapy, which may only require a singular injection every 10 years.[109-111] IVT delivery would greatly diminish the possibility of retinal iatrogenic damage, the need for general anesthesia during surgery, and the need for additional surgical training programs. This would widely expand the population of individuals that can be treated with this therapy. While AAV production remains expensive, these factors bring us closer to making this type of therapy more available.

Overall, we are most excited to demonstrate cross species consistency of AAV2.Var3 RPE transduction in this study. Without signs of toxicity or ocular inflammation across all 12 weeks of post-surgical observation, there is high translatability of this novel capsid. There is a strong need for more characterization of this capsid to discover the limiting factors. For now, we are compelled that the capsid is a large step forward in the field of AAV-mediated gene therapy for retinal degenerative diseases and see a future of IVT delivery for patients.

Bibliography

1 Xie, Q. *et al.* The atomic structure of adeno-associated virus (AAV-2), a vector for human gene therapy. *Proc Natl Acad Sci U S A* **99**, 10405-10410 (2002). https://doi.org/10.1073/pnas.162250899

2 Liu, F., Li, R., Zhu, Z., Yang, Y. & Lu, F. Current developments of gene therapy in human diseases. *MedComm* **5**, e645 (2024). https://doi.org/10.1002/mco2.645

3 Eric Hastie, R. J. S. Adeno-Associated Virus at 50: A Golden Anniversary of Discovery, Research, and Gene Therapy Success—A Personal Perspective. *Adeno-Associated Virus* (2015).

4 Duong, T. T. *et al.* Comparative AAV-eGFP Transgene Expression Using Vector Serotypes 1-9, 7m8, and 8b in Human Pluripotent Stem Cells, RPEs, and Human and Rat Cortical Neurons. *Stem Cells Int.* **2019**, 7281912 (2019). https://doi.org/10.1155/2019/7281912

5 Büning, H. & Srivastava, A. Capsid modifications for targeting and improving the efficacy of AAV vectors. *Mol. Ther. Methods Clin. Dev.* **12**, 248-265 (2019). https://doi.org/10.1016/j.omtm.2019.01.008

6 Luo, N.-S. *et al.* Engineered AAV13 variants with enhanced transduction and confined spread. *Zool. Res.* **45**, 781-790 (2024). https://doi.org/10.24272/j.issn.2095-8137.2023.355

7 Ponnazhagan, S., Mahendra, G., Kumar, S., Thompson, J. A. & Castillas, M. Conjugate-based targeting of recombinant adeno-associated virus type 2 vectors by using avidin-linked ligands. *J Virol* **76**, 12900-12907 (2002). https://doi.org/10.1128/jvi.76.24.12900-12907.2002

8 Zhang, R. *et al.* Adeno-associated virus 2 bound to its cellular receptor AAVR. *Nat. Microbiol.* **4**, 675-682 (2019). https://doi.org/10.1038/s41564-018-0356-7

9 Opie, S. R., Warrington, K. H., Jr., Agbandje-McKenna, M., Zolotukhin, S. & Muzyczka, N. Identification of amino acid residues in the capsid proteins of adeno-associated virus type 2 that contribute to heparan sulfate proteoglycan binding. *J. Virol.* **77**, 6995-7006 (2003). https://doi.org/10.1128/jvi.77.12.6995-7006.2003

10 Flannery, J. G. & Visel, M. Adeno-associated viral vectors for gene therapy of inherited retinal degenerations. *Methods Mol. Biol.* **935**, 351-369 (2013). https://doi.org/10.1007/978-1-62703-080-9_25

11 Kotterman, M. A. & Schaffer, D. V. Engineering adeno-associated viruses for clinical gene therapy. *Nat. Rev. Genet.* **15**, 445-451 (2014). https://doi.org/10.1038/nrg3742

12 Li, C. & Samulski, R. J. Engineering adeno-associated virus vectors for gene therapy. *Nat. Rev. Genet.* **21**, 255-272 (2020). https://doi.org/10.1038/s41576-019-0205-4

13 Rayaprolu, V. *et al.* Comparative Analysis of Adeno-Associated Virus Capsid Stability and Dynamics. *J. Virol.* **87**, 13150-13160 (2013). https://doi.org/10.1128/jvi.01415-13

14 Bijlani, S., Pang, K. M., Sivanandam, V., Singh, A. & Chatterjee, S. The Role of Recombinant AAV in Precise Genome Editing. *Front Genome Ed* **3**, 799722 (2021). https://doi.org/10.3389/fgeed.2021.799722

15 Masland, R. H. The fundamental plan of the retina. *Nat Neurosci* **4**, 877-886 (2001). https://doi.org/10.1038/nn0901-877

16 Manley, A., Meshkat, B. I., Jablonski, M. M. & Hollingsworth, T. J. Cellular and molecular mechanisms of pathogenesis underlying inherited retinal dystrophies. *Biomolecules* **13**, 271 (2023). https://doi.org/10.3390/biom13020271

17 Curcio, C. A., Sloan, K. R., Kalina, R. E. & Hendrickson, A. E. Human photoreceptor topography. *J. Comp. Neurol.* **292**, 497-523 (1990). https://doi.org/10.1002/cne.902920402

18 D, P., GJ, A. & D, F. (Sinauer Associates, Neuroscience, 2001).

19 Volland, S., Esteve-Rudd, J., Hoo, J., Yee, C. & Williams, D. S. A comparison of some organizational characteristics of the mouse central retina and the human macula. *PLoS One* **10**, e0125631 (2015). https://doi.org/10.1371/journal.pone.0125631

20 Stoddart, P. R., Begeng, J. M., Tong, W., Ibbotson, M. R. & Kameneva, T. Nanoparticle-based optical interfaces for retinal neuromodulation: a review. *Front. Cell. Neurosci.* **18**, 1360870 (2024). https://doi.org/10.3389/fncel.2024.1360870

21 Strauss, O. The retinal pigment epithelium in visual function. *Physiol. Rev.* **85**, 845-881 (2005). https://doi.org/10.1152/physrev.00021.2004

22 Leroy, B. P. *et al.* Gene therapy for inherited retinal disease: Long-term durability of effect. *Ophthalmic Res.* **66**, 179-196 (2023). https://doi.org/10.1159/000526317

23 Kolesnikov, A. V., Tang, P. H. & Kefalov, V. J. Examining the Role of Cone-expressed RPE65 in Mouse Cone Function. *Sci. Rep.* (2018). https://doi.org/10.1038/s41598-018-32667-w

24 Pang, J.-J. *et al.* Gene therapy restores vision-dependent behavior as well as retinal structure and function in a mouse model of RPE65 Leber congenital amaurosis. *Mol. Ther.* **13**, 565-572 (2006). https://doi.org/10.1016/j.ymthe.2005.09.001

25 Boye, S. L. *et al.* Novel AAV44.9-based vectors display exceptional characteristics for retinal gene therapy. *Mol. Ther.* **28**, 1464-1478 (2020). https://doi.org/10.1016/j.ymthe.2020.04.002

26 Nash, B. M., Wright, D. C., Grigg, J. R., Bennetts, B. & Jamieson, R. V. Retinal dystrophies, genomic applications in diagnosis and prospects for therapy. *Transl. Pediatr.* **4**, 139-163 (2015). https://doi.org/10.3978/j.issn.2224-4336.2015.04.03

27 Kumaran, N., Moore, A. T., Weleber, R. G. & Michaelides, M. Leber congenital amaurosis/early-onset severe retinal dystrophy: clinical features, molecular genetics and therapeutic interventions. *Br. J. Ophthalmol.* **101**, 1147-1154 (2017). https://doi.org/10.1136/bjophthalmol-2016-309975

28 Imanishi, Y., Batten, M. L., Piston, D. W., Baehr, W. & Palczewski, K. Noninvasive two-photon imaging reveals retinyl ester storage structures in the eye. *J. Cell Biol.* **164**, 373-383 (2004). https://doi.org/10.1083/jcb.200311079

29 Van Hooser, J. P. *et al.* Recovery of visual functions in a mouse model of Leber congenital amaurosis. *J. Biol. Chem.* **277**, 19173-19182 (2002). https://doi.org/10.1074/jbc.M112384200

30 Cideciyan, A. V. *et al.* Human retinal gene therapy for Leber congenital amaurosis shows advancing retinal degeneration despite enduring visual improvement. *Proc. Natl. Acad. Sci. U. S. A.* **110** (2013). https://doi.org/10.1073/pnas.1218933110

31 Liu, Y. *et al.* Unlocking therapeutic potential: dual gene therapy for ameliorating the disease phenotypes in a mouse model of RPE65 Leber congenital amaurosis. *Front. Med. (Lausanne)* **10** (2024). https://doi.org/10.3389/fmed.2023.1291795

32 Hageman, G. S. *et al.* A common haplotype in the complement regulatory gene factor H (HF1/CFH) predisposes individuals to age-related macular degeneration. *Proc. Natl. Acad. Sci. U. S. A.* **102**, 7227-7232 (2005). https://doi.org/10.1073/pnas.0501536102

33 Mandal, M. N. A. & Ayyagari, R. Complement factor H: spatial and temporal expression and localization in the eye. *Invest. Ophthalmol. Vis. Sci.* **47**, 4091-4097 (2006). https://doi.org/10.1167/iovs.05-1655

34 Clark, S. J. & Bishop, P. N. The eye as a complement dysregulation hotspot. *Semin Immunopathol* **40**, 65-74 (2018). https://doi.org/10.1007/s00281-017-0649-6

35 Clark, S. J. *et al.* Impaired binding of the age-related macular degeneration-associated complement factor H 402H allotype to Bruch's membrane in human retina. *J. Biol. Chem.* **285**, 30192-30202 (2010). https://doi.org/10.1074/jbc.M110.103986

36 Klein, R. J. *et al.* Complement factor H polymorphism in age-related macular degeneration. *Science* **308**, 385-389 (2005). https://doi.org/10.1126/science.1109557

37 Rafieetary, S. & Huddleston, S. Gene therapy delivery: Examining the evidence. (2023).

38 Ross, M. & Ofri, R. The future of retinal gene therapy: evolving from subretinal to intravitreal vector delivery. *Neural Regeneration Res.* **16**, 1751-1759 (2021). https://doi.org/10.4103/1673-5374.306063

39 Dalkara, D. *et al.* In vivo-directed evolution of a new adeno-associated virus for therapeutic outer retinal gene delivery from the vitreous. *Sci. Transl. Med.* **5**, 189ra176 (2013). https://doi.org/10.1126/scitranslmed.3005708

40 Han, I. C. *et al.* Retinal tropism and transduction of adeno-associated virus varies by serotype and route of delivery (intravitreal, subretinal, or suprachoroidal) in rats. *Hum. Gene Ther.* **31**, 1288-1299 (2020). https://doi.org/10.1089/hum.2020.043

41 L'Abbate, D., Prescott, K., Geraghty, B., Kearns, V. R. & Steel, D. H. W. Biomechanical considerations for optimising subretinal injections. *Surv. Ophthalmol.* **69**, 722-732 (2024). https://doi.org/10.1016/j.survophthal.2024.05.004

42 Russell, S. *et al.* Efficacy and safety of voretigene neparvovec (AAV2-hRPE65v2) in patients with RPE65-mediated inherited retinal dystrophy: a randomised, controlled, open-label, phase 3 trial. *Lancet* **390**, 849-860 (2017). https://doi.org/10.1016/S0140-6736(17)31868-8

43 Kolesnikova, M. *et al.* Chorioretinal atrophy following voretigene neparvovec despite the presence of fundus autofluorescence. *Mol. Genet. Genomic Med.* **10**, e2038 (2022). https://doi.org/10.1002/mgg3.2038

44 Gange, W. S. *et al.* Perifoveal chorioretinal atrophy after subretinal voretigene neparvovec-rzyl for RPE65-mediated Leber congenital amaurosis. *Ophthalmol. Retina* **6**, 58-64 (2022). https://doi.org/10.1016/j.oret.2021.03.016

45 Bommakanti, N. *et al.* Classification and growth rate of chorioretinal atrophy after voretigene neparvovec-rzyl for RPE65-mediated retinal degeneration. *Ophthalmol. Retina* **8**, 42-48 (2024). https://doi.org/10.1016/j.oret.2023.08.017

46 Lorenz, B. *et al.* Single center experience with voretigene neparvovec gene augmentation therapy in RPE65 mutation-associated inherited retinal degeneration in a clinical setting. *Ophthalmology* **131**, 161-178 (2024). https://doi.org/10.1016/j.ophtha.2023.09.006

47 Stingl, K. *et al.* Full-field scotopic threshold improvement after voretigene neparvovec-rzyl treatment correlates with chorioretinal atrophy. *Ophthalmology* **130**, 764-770 (2023). https://doi.org/10.1016/j.ophtha.2023.02.015

48 Fischer, M. D. *et al.* Real-world safety and effectiveness of voretigene neparvovec: Results up to 2 years from the prospective, registry-based PERCEIVE study. *Biomolecules* **14**, 122 (2024). https://doi.org/10.3390/biom14010122

49 Huang, P. *et al.* Subretinal injection in mice to study retinal physiology and disease. *Nat. Protoc.* **17**, 1468-1485 (2022). https://doi.org/10.1038/s41596-022-00689-4

50 Bruewer, A. R. *et al.* Evaluation of lateral spread of transgene expression following subretinal AAV-mediated gene delivery in dogs. *PLoS One* **8**, e60218 (2013). https://doi.org/10.1371/journal.pone.0060218

51 Garafalo, A. V. *et al.* Progress in treating inherited retinal diseases: Early subretinal gene therapy clinical trials and candidates for future initiatives. *Prog. Retin. Eye Res.* **77**, 100827 (2020). https://doi.org/10.1016/j.preteyeres.2019.100827

52 Ong, T., Pennesi, M. E., Birch, D. G., Lam, B. L. & Tsang, S. H. Adeno-associated viral gene therapy for inherited retinal disease. *Pharm. Res.* **36**, 34 (2019). https://doi.org/10.1007/s11095-018-2564-5

53 Dalkara, D. *et al.* Inner Limiting Membrane Barriers to AAV-mediated Retinal Transduction From the Vitreous. *Mol. Ther.* **17**, 2096-2102 (2009). https://doi.org/10.1038/mt.2009.181

54 Inatani, M. & Tanihara, H. Proteoglycans in retina. *Prog. Retin. Eye Res.* **21**, 429-447 (2002). https://doi.org/10.1016/s1350-9462(02)00009-5

55 Inatani, M. *et al.* Spatiotemporal expression patterns of N-syndecan, a transmembrane heparan sulfate proteoglycan, in developing retina. *Invest. Ophthalmol. Vis. Sci.* **43**, 1616-1621 (2002).

56 Boye, S. L. *et al.* Impact of heparan sulfate binding on transduction of retina by recombinant adeno-associated virus vectors. *J. Virol.* **90**, 4215-4231 (2016). https://doi.org/10.1128/JVI.00200-16

57 Wu, Z. *et al.* Single amino acid changes can influence titer, heparin binding, and tissue tropism in different adeno-associated virus serotypes. *J. Virol.* **80**, 11393-11397 (2006). https://doi.org/10.1128/JVI.01288-06

58 Li, W. *et al.* Engineering and Selection of Shuffled AAV Genomes: A New Strategy for Producing Targeted Biological Nanoparticles. *Mol Ther* **16**, 1252-1260 (2008). https://doi.org/10.1038/mt.2008.100

59 Wu, P. *et al.* Mutational analysis of the adeno-associated virus type 2 (AAV2) capsid gene and construction of AAV2 vectors with altered tropism. *J. Virol.* **74**, 8635-8647 (2000). https://doi.org/10.1128/jvi.74.18.8635-8647.2000

60 Shi, W. & Bartlett, A. Insertional mutagenesis adeno-associated virus type 2 (AAV2) capsid gene generation 30 AAV2 vectors targeted alternative cell-surface receptors. *Hum Gene Ther* **12**, 1697-1711 (2001).

61 Yiu, G., Chung, S. H., Mollhoff, I., Nguyen, U. T. & Thomasy, S. M. Host immune responses to suprachoroidal AAV8 injections for ocular gene delivery in nonhuman primates. *Invest. Ophthalmol. Vis. Sci.* **61**, 2294-2294 (2020).

62 Byrne, L. C., Lin, Y. J., Lee, T., Schaffer, D. V. & Flannery, J. G. The expression pattern of systemically injected AAV9 in the developing mouse retina is determined by age. *Mol. Ther.* **23**, 290-296 (2015). https://doi.org/10.1038/mt.2014.181

63 Bennett, J., Duan, D., Engelhardt, J. F. & Maguire, A. M. Real-time, noninvasive in vivo assessment of adeno-associated virus-mediated retinal transduction. *Invest Ophthalmol Vis Sci* **38**, 2857-2863 (1997).

64 Flannery, J. G. *et al.* Efficient photoreceptor-targeted gene expression in vivo by recombinant adeno-associated virus. *Proc Natl Acad Sci U S A* **94**, 6916-6921 (1997). https://doi.org/10.1073/pnas.94.13.6916

65 Bennett, J. Overview of Retinal Gene Therapy: Current Status and Future Challenges. *Cold Spring Harb Perspect Med* **13** (2023). https://doi.org/10.1101/cshperspect.a041278

66 Lee, G. K., Maheshri, N., Kaspar, B. & Schaffer, D. V. PEG conjugation moderately protects adeno-associated viral vectors against antibody neutralization. *Biotechnol. Bioeng.* **92**, 24-34 (2005). https://doi.org/10.1002/bit.20562

67 Kern, A. *et al.* Identification of a heparin-binding motif on adeno-associated virus type 2 capsids. *J. Virol.* **77**, 11072-11081 (2003). https://doi.org/10.1128/jvi.77.20.11072-11081.2003

68 Girod, A. *et al.* Genetic capsid modifications allow efficient re-targeting of adeno-associated virus type 2. *Nat Med* **5**, 1438 (1999). https://doi.org/10.1038/71021

69 Müller, O. J. *et al.* Random peptide libraries displayed on adeno-associated virus to select for targeted gene therapy vectors. *Nat. Biotechnol.* **21**, 1040-1046 (2003). https://doi.org/10.1038/nbt856

70 Naumer, M., Popa-Wagner, R. & Kleinschmidt, J. A. Impact of capsid modifications by selected peptide ligands on recombinant adeno-associated virus serotype 2-mediated gene transduction. *J Gen Virol* **93**, 2131-2141 (2012). https://doi.org/10.1099/vir.0.044735-0

71 Perabo, L. *et al.* In vitro selection of viral vectors with modified tropism: the adeno-associated virus display. *Mol Ther* **8**, 151-157 (2003). https://doi.org/10.1016/s1525-0016(03)00123-0

72 Öztürk, B. E. *et al.* scAAVengr, a transcriptome-based pipeline for quantitative ranking of engineered AAVs with single-cell resolution. *Elife* **10** (2021). https://doi.org/10.7554/eLife.64175

73 Khabou, H. *et al.* Insight into the mechanisms of enhanced retinal transduction by the engineered AAV2 capsid variant -7m8. *Biotechnol. Bioeng.* **113**, 2712-2724 (2016). https://doi.org/10.1002/bit.26031

74 Koerber, J. T., Maheshri, N., Kaspar, B. K. & Schaffer, D. V. Construction of diverse adeno-associated viral libraries for directed evolution of enhanced gene delivery vehicles. *Nat. Protoc.* **1**, 701-706 (2006). https://doi.org/10.1038/nprot.2006.93

75 Byrne, L. C. *et al.* In vivo-directed evolution of adeno-associated virus in the primate retina. *JCI Insight* **5** (2020). https://doi.org/10.1172/jci.insight.135112

76 Koerber, J. T., Jang, J.-H. & Schaffer, D. V. DNA shuffling of adeno-associated virus yields functionally diverse viral progeny. *Mol. Ther.* **16**, 1703-1709 (2008). https://doi.org/10.1038/mt.2008.167

77 Kaludov, N., Brown, K. E., Walters, R. W., Zabner, J. & Chiorini, J. A. Adeno-associated virus serotype 4 (AAV4) and AAV5 both require sialic acid binding for hemagglutination and efficient transduction but differ in sialic acid linkage specificity. *J Virol* **75**, 6884-6893 (2001). https://doi.org/10.1128/JVI.75.15.6884-6893.2001

78 Lotery, A. J. *et al.* Adeno-associated virus type 5: transduction efficiency and cell-type specificity in the primate retina. *Hum Gene Ther* **14**, 1663-1671 (2003). https://doi.org/10.1089/104303403322542301

79 Peden, C. S., Burger, C., Muzyczka, N. & Mandel, R. J. Circulating anti-wild-type adeno-associated virus type 2 (AAV2) antibodies inhibit recombinant AAV2 (rAAV2)-mediated, but not rAAV5-mediated, gene transfer in the brain. *J Virol* **78**, 6344-6359 (2004). https://doi.org/10.1128/JVI.78.12.6344-6359.2004

80 Weber, M. *et al.* Recombinant adeno-associated virus serotype 4 mediates unique and exclusive long-term transduction of retinal pigmented epithelium in rat, dog, and nonhuman primate after subretinal delivery. *Mol Ther* **7**, 774-781 (2003). https://doi.org/10.1016/s1525-0016(03)00098-4

81 Gonzalez-Cordero, A. *et al.* Assessment of AAV Vector Tropisms for Mouse and Human Pluripotent Stem Cell-Derived RPE and Photoreceptor Cells. *Hum Gene Ther* **29**, 1124-1139 (2018). https://doi.org/10.1089/hum.2018.027

82 Wright, J. F. Product-Related Impurities in Clinical-Grade Recombinant AAV Vectors: Characterization and Risk Assessment. *Biomedicines* **2**, 80-97 (2014). https://doi.org/10.3390/biomedicines2010080

83 Mingozzi, F. & High, K. A. Immune responses to AAV in clinical trials. *Curr Gene Ther* **11**, 321-330 (2011). https://doi.org/10.2174/156652311796150354

84 Mingozzi, F. & High, K. A. Therapeutic in vivo gene transfer for genetic disease using AAV: progress and challenges. *Nat Rev Genet* **12**, 341-355 (2011). https://doi.org/10.1038/nrg2988

85 Wright, J. F. AAV empty capsids: for better or for worse? *Mol Ther* **22**, 1-2 (2014). https://doi.org/10.1038/mt.2013.268

86 Bennett, A. *et al.* Structure comparison of the chimeric AAV2.7m8 vector with parental AAV2. *Journal of Structural Biology* **209**, 107433 (2020). https://doi.org/10.1016/j.jsb.2019.107433

87 De Clerck, K., De Smedt, S., Remaut, K. & Peynshaert, K. Toward successful retinal drug delivery after intravitreal injection: Current strategies to overcome the inner limiting membrane. *J. Control. Release*, 113849 (2025). https://doi.org/10.1016/j.jconrel.2025.113849

88 Peynshaert, K., Devoldere, J., Minnaert, A. K., De Smedt, S. C. & Remaut, K. Morphology and Composition of the Inner Limiting Membrane: Species-Specific Variations and Relevance toward Drug Delivery Research. *Curr Eye Res* **44**, 465-475 (2019). https://doi.org/10.1080/02713683.2019.1565890

89 Okanouchi, T., Toshima, S., Kimura, S., Morizane, Y. & Shiraga, F. Novel Technique for Subretinal Injection Using Local Removal of the Internal Limiting Membrane. *Retina* **36**, 1035-1038 (2016). https://doi.org/10.1097/IAE.0000000000001029

90 Parida, H., Kannan, N. B. & Rathinam, S. R. Imaging of Muller cell sheen dystrophy. *Indian J Ophthalmol* **68**, 533-535 (2020). https://doi.org/10.4103/ijo.IJO_930_19

91 Kim, T.-H., Weimer, R. & Elstrott, J. Cellular-resolution OCT reveals layer-specific retinal mosaics and ganglion cell degeneration in mouse retina in vivo. *Neurophotonics* **13**, 015006 (2026). https://doi.org/10.1117/1.NPh.13.1.015006

92 Adini, I. & Ghosh, K. Mouse retinal whole mounts and quantification of vasculature protocol. *Bio Protoc.* **5** (2015). https://doi.org/10.21769/bioprotoc.1546

93 Cideciyan, A. V. *et al.* Human gene therapy for RPE65 isomerase deficiency activates the retinoid cycle of vision but with slow rod kinetics. *Proc. Natl. Acad. Sci. U. S. A.* **105**, 15112-15117 (2008). https://doi.org/10.1073/pnas.0807027105

94 Hauswirth, W. W. *et al.* Treatment of leber congenital amaurosis due to RPE65 mutations by ocular subretinal injection of adeno-associated virus gene vector: short-term results of a phase I trial. *Hum. Gene Ther.* **19**, 979-990 (2008). https://doi.org/10.1089/hum.2008.107

95 Bainbridge, J. W. B. *et al.* Effect of gene therapy on visual function in Leber's congenital amaurosis. *N. Engl. J. Med.* **358**, 2231-2239 (2008). https://doi.org/10.1056/NEJMoa0802268

96 Sather, R., Ihinger, J., Simmons, M., Lobo, G. P. & Montezuma, S. R. The Clinical Findings, Pathogenic Variants, and Gene Therapy Qualifications Found in a Leber Congenital Amaurosis Phenotypic Spectrum Patient Cohort. *Int. J. Mol. Sci.* **25**, 1253 (2024). https://doi.org/10.3390/ijms25021253

97 Pang, J. *et al.* Retinal degeneration 12 (rd12): a new, spontaneously arising mouse model for human Leber congenital amaurosis (LCA). *Mol. Vis.* **11**, 152-162 (2005).

98 Li, X. *et al.* Gene therapy rescues cone structure and function in the 3-month-old rd12 mouse: a model for midcourse RPE65 leber congenital amaurosis. *Invest. Ophthalmol. Vis. Sci.* **52**, 7-15 (2011). https://doi.org/10.1167/iovs.10-6138

99 Jeon, C. J., Strettoi, E. & Masland, R. H. The major cell populations of the mouse retina. *J. Neurosci.* **18**, 8936-8946 (1998). https://doi.org/10.1523/jneurosci.18-21-08936.1998

100 Choi, E. H. *et al.* In vivo base editing rescues cone photoreceptors in a mouse model of early-onset inherited retinal degeneration. *Nat. Commun.* **13**, 1830 (2022). https://doi.org/10.1038/s41467-022-29490-3

101 Xiong, W. *et al.* AAV. *Proc Natl Acad Sci U S A* **116**, 5785-5794 (2019). https://doi.org/10.1073/pnas.1821000116

102 Liu, Z. *et al.* The clinical safety landscape for ocular AAV gene therapies: A systematic review and meta-analysis. *iScience.* **28**, 112265. doi: 112210.111016/j.isci.112025.112265. eCollection 112025 Apr 112218.

103 Wiley, L. A.-O. *et al.* in *Hum Gene Ther.* Vol. 34 530-539. doi: 510.1089/hum.2022.1222. Epub 2023 Mar 1028.

104 Wang, Y., Wang, V. M. & Chan, C. C. The role of anti-inflammatory agents in age-related macular degeneration (AMD) treatment. *Eye* **25**, 127-139 (2011). https://doi.org/10.1038/eye.2010.196

105 Ramachandran, P. S. *et al.* Evaluation of dose and safety of AAV7m8 and AAV8BP2 in the non-human primate retina. *Hum. Gene Ther.* **28**, 154-167 (2017). https://doi.org/10.1089/hum.2016.111

106 Golczak, M., Bereta, G., Maeda, A. & Palczewski, K. Molecular biology and analytical chemistry methods used to probe the retinoid cycle. *Methods Mol. Biol.* **652**, 229-245 (2010). https://doi.org/10.1007/978-1-60327-325-1_13

107 Engfer, Z. J. *et al.* Retinol tracing within murine neural retina reveals cell type-specific retinol transport and distribution. *J. Clin. Invest.* (2025). https://doi.org/10.1172/jci198648

108 Lin, C. H. *et al.* A protocol to inject ocular drug implants into mouse eyes. *STAR Protoc* **3**, 101143 (2022). https://doi.org/10.1016/j.xpro.2022.101143

109 Marcó, S. *et al.* Seven-year follow-up of durability and safety of AAV CNS gene therapy for a lysosomal storage disorder in a large animal. *Mol Ther Methods Clin Dev* **23**, 370-389 (2021).

110 Nguyen, G. N. *et al.* in *Nat Biotechnol.* Vol. 39 47-55. doi: 10.1038/s41587-41020-40741-41587. Epub 42020 Nov 41516.

111 Buchlis, G. *et al.* in *Blood.* Vol. 119 3038-3041. doi: 3010.1182/blood-2011-3009-382317. Epub 382012 Jan 382323.